Geophysical Investigation of a Geologic Unconformity at Seward Park - Seattle, WA

Kevin J. Cowell

A report prepared in partial fulfillment of
the requirements for the degree of

Master of Science
Earth and Space Sciences: Applied Geosciences

University of Washington
June, 2018

Project mentor:
Recep (Ray) Cakir, Washington Geological Survey

Internship coordinator:
Kathy Troost

Reading committee:
Kathy Troost
Juliet Crider

MESSAGe Technical Report Number: [068]

Executive Summary

This report presents the results of field and geophysical analyses of a geologic unconformity located within Seattle's Seward Park. The unconformity consists of an apparently abrupt contact between Quaternary Vashon till in the north and Tertiary bedrock to the south. Seward Park is located in the middle of the Seattle Fault Zone (SFZ). The SFZ is an active crustal fault capable of producing M_w7+ earthquakes, triggering tsunamis in Puget Sound, and causing ground deformation. Previous interpretations of regional fault zone imaging indicate the possible presence of a fault strand in Seward Park. Methods of geophysical analysis used in my study include seismic refraction, multichannel analysis of surface waves (MASW), and ground-penetrating radar (GPR). Data results include a compressional velocity (V_p) model, shear velocity (V_s) model, and a radargram. These results were used to interpret the nature of the unconformity at depth. This information was then coupled with surficial geologic observations in order to develop suitable interpretations. The data results depict an abrupt transition in seismic velocities within the measured transects. Three potential geologic mechanisms have been proposed to explain this phenomenon. One scenario, consistent with interpretations from previous studies, is a fault-generated unconformity caused by a south-side-up thrust fault dipping (20-30^o) to the south. A second possibility: the unconformity was formed via one or multiple erosional processes. Third, the bedrock was deformed before Quaternary deposition and the contact represents a buttress unconformity. Additional work is required in order to confirm or refute these geologic scenarios. Recommendations for future work include utilizing seismic reflection in order to image this location at greater depth, running longer geophysical arrays, measuring another transect in the middle of the Bailey Peninsula, and conducting borehole analyses or trenching. Limitations of this study include sparse surficial data, depth of geophysical penetration, topographic constraints, and limited survey extent due to time factors.

Acknowledgements

This project was completed thanks to the help and contributions of several individuals. I would like to thank Kathy Troost for initially proposing this project and providing intellectual guidance; Ray (Recep) Cakir from the Washington Geological Survey for the devotion of his expertise, time, and geophysical equipment without which this project would not have been possible; Jesse Martinez from Northwest Geophysics LLC for his help in the completion of this project; Dean Goodman of GPR-Slice for access to the GPR-Slice software; Austin Rains for his work and data contributions; and Juliet Crider for her aid in the revision process. I would also like to acknowledge the Wilbert R. Danner Fund for its contributions to my education.

Table of Contents

List of Figures

List of Appendices

1.0 Introduction

Seattle, Washington lies within the Puget Lowland, a region that has experienced multiple shallow crustal earthquakes over the past several thousand years (Sherrod and Gomberg, 2014). Many fault systems are located within the Puget Lowland (Figure 1). The Seattle Fault Zone (SFZ) is one such fault system that traverses south Seattle and comprises a series of shallow E-W trending thrust and back thrust faults (Figure 2). Paleoseismic research has revealed that a large crustal earthquake, likely originating from the SFZ, occurred approximately 1-1.1 ka triggering ground deformation and a tsunami within Puget Sound (Atwater and Moore, 1992). It has also been determined that the SFZ is currently experiencing a slip rate of 0.7-1.1 mm/year implying the potential to reproduce a M_w7+ seismic event (Johnson et. al, 1999). The SFZ introduces an innate seismic hazard, and therefore its identification and characterization aids scientists and engineers in mitigating major seismic events. Fault location, displacement, geometry, and slip rate are all key parameters essential for earthquake hazard assessments (Johnson et al., 1999). Given the current geologic parameters, the Earthquake Engineering Research Institute (2005) has predicted that an M_w 6.7 earthquake along the SFZ could generate enough energy to produce ground motions 2-5 times that of the 2001 Nisqually earthquake. Unfortunately, due to dense vegetation, urban sprawl, and land modifications in urban areas like Seattle, the locations and orientations of SFZ strands are still poorly understood. This problem can be overcome by combining geophysical methods with surface geologic observations to better determine fault strand positioning.

2.0 Scope of Work

The focus of this project is to convey the results of seismic refraction, multichannel analysis of surface waves (MASW), and ground-penetrating radar (GPR) surveys conducted in Seattle's Seward Park (Figure 3). The results from these shallow geophysical techniques are used to interpret the subsurface near an unconformable contact between Oligocene-Miocene aged Blakeley Formation sandstone and Quaternary aged Vashon till. While the origin of this unconformity has yet to be explained, one hypothesis consistent with other regional studies is that the abrupt contact is a result of displacement along a south-side-up reverse fault. If this proves to be true, Seward Park presents a rare opportunity to constrain the position and geometry of a fault strand in a location not

yet modified by city infrastructure. Geophysical techniques are often capable of delineating subsurface stratigraphy in a non-invasive manner. Contrasts in the dielectric, and/or elastic properties between the two geologic units may elucidate the geometry of this contact. I determined survey transect locations based on direct observations made in the field. This included collecting attitude measurements of the surficial geology in addition to field estimates of rock strength, fracture density, and other potential influences on the modeled results. I also processed geophysical survey data to generate models and interpretations of the subsurface based off of the parameters described above.

3.0 Geologic Setting

3.1 Puget Lowland

Seattle, Washington lies within the Puget Lowland, an area characterized by complex geology as a result of past glaciations and active tectonics (Troost and Booth, 2008). The oblique subduction of the Juan de Fuca plate beneath North America results in a northeasterly migration of coastal Washington State relative to North America (Figure 4) (McCaffery et al., 2007). Faulting occurs within the Puget Lowland due to crustal shortening of accretionary and glacially derived materials that are relatively incompetent in comparison to the cratonic rock of southwest Canada (Lamb et al., 2012). The Vashon Glaciation is the last to have occupied the Puget Lowland. The glacier reached its southernmost extent near Olympia, WA ca. 16,950 Cal yrs B.P. (Porter and Swanson, 1998). The glacier was 1000 meters thick where Seattle sits today and left behind deposits of till, sand and gravel, and lacustrine silt and clay (Troost and Booth, 2005). Recent glacial processes also produced many geomorphic features such as drumlins, steep coastal bluffs, and deeply incised troughs.

3.2 Seattle Fault Zone (SFZ) Structure

The SFZ consists of a swath of east-west-trending, subparallel fault strands (Sherrod and Gomberg, 2014; Pratt et al., 2015). Many of these strands have been discovered by investigative studies relying on high-resolution aeromagnetic, gravity, and seismic reflection data (Sherrod and Gomberg, 2014; Pratt et al, 2015). South of the deformation front, uplifted Tertiary rocks are located at the surface in a few locations. To the north, the Seattle Basin is filled with Quaternary glacial and interglacial sediment. The difference in material density produces a strong gravitational anomaly that is detectable by geophysical methods (Danes et al., 1965). The SFZ is generally

understood to contain a set of south-side-up imbricated thrust faults (Blakely et al., 2009; Johnson et al., 1994, 1999; Brink et al., 2002; Brocher et al., 2004). However, its exact geometry is not well defined. Johnson et al. (1999) has suggested that these fault strands are split into two primary segments by a N-S trending strike-slip fault that has experienced 2.4 km of dextral displacement. Pratt et al. (1997) initially determined that a wedge model could be an appropriate analog, while more recent research conducted by Liberty and Pratt (2008) and Pratt et al. (2015) interpret the SFZ to be a consequence of a fault-propagation fold. In addition to the main thrust faults, evidence for north-side-up back thrusts has also been found (Pratt et al., 2015). Research of particular relevance to this study includes that performed near Seward Park. Seward Park is coterminous with the Bailey Peninsula, an undeveloped plot of land that protrudes into southwestern Lake Washington. Geophysical data collected at Mercer Island has caused speculation that Quaternary faulting may trend through the island on a trajectory that would also cross the Bailey Peninsula (Figure 5) (Harding et al, 1998; Blakely et al., 2002; Stephenson et al., 2007). The cause of this speculation was the lack of reflective surfaces normally produced by the Quaternary stratigraphy (Figure 6).

3.3 Seattle Fault Zone (SFZ) Paleoseismicity

While many studies have worked to better describe the SFZ, paleoseismic studies have discovered evidence for SFZ seismic activity (Atwater and Moore 1992; Bucknam et al., 1992; Jacoby et al., 1992; Karlin and Abella, 1996; Huntley and Clague, 1996; Sherrod, 2000; Bourgeois and Johnson, 2001; Karlin et al., 2004; Martin and Bourgeois, 2011). Several sources point to evidence of a large Seattle fault earthquake occurring approximately 1,100 years ago. Atwater and Moore (1992) made a significant discovery near the northwestern head of Cultus Bay when they found evidence of earthquake-generated tsunami deposits sourced from the Puget Sound. Since 1992, several additional studies have corroborated this finding using multiple paleoseismic techniques (Bucknam et al., 1992; Sherrod et al., 2000; Nelson et al., 2003; Kelsey et al., 2008). One of the most significant pieces of evidence was collected on a raised intertidal platform bordering the shoreline of Bainbridge Island (Figure 7). Sediment cores collected at this location show an abrupt shift from tide flat diatoms to freshwater taxa indicating an uplift of 7-8 meters during the same time period as this earthquake event (Sherrod, 2000).

3.4 Seward Park/Bailey Peninsula

Seward Park is a municipal park located on the Bailey Peninsula in southeast Seattle, Washington (Figure 3). The Bailey Peninsula encompasses a 300-acre plot of land that juts into the southern end of Lake Washington (Talbert, 2017). Vashon till is found in the northern half of the Bailey Peninsula while Tertiary bedrock exists in the south (Figure 8). This Tertiary bedrock, part of the Blakeley Formation, was deposited at the Oligocene-Miocene boundary. It consists of marine sedimentary and volcanoclastic rocks deposited in a shallow marine or near shore environment (Troost and Booth, 2008). At the surface, this bedrock is saprolitic and difficult to identify when in contact with Vashon till due to weathering and mixing at the contact. In some instances, the Vashon till is harder than the weathered bedrock (Williams et al., 1999; Savage et al., 2000; Troost and Booth, 2008; Wong et al., 2011). Several scarp features and high bluffs are visible along the margins of the peninsula (Figures 8). It is possible that some of these features were developed via a co-seismic landslide event (Karlin et al., 2004). In addition, a quarry that once existed on the west side of the park could be the origin of some of the steep scarp features (Talbert, personal communication, 2018). The contact between till and bedrock in Seward Park has been mapped as striking E-W (Troost et al., 2005). This orientation aligns with the geometry of known faults found throughout the region and is the basis for the hypothesis that the contact is a fault strand.

4.0 Field Methods

4.1 Objectives

I performed field work in order to meet four primary goals: 1) to describe the strength, weathering, and engineering properties of the Tertiary bedrock, 2) to determine the attitude of bedding in the Tertiary bedrock, 3) to better delineate the location of the till/bedrock in outcrop, and 4) to select appropriate survey transects for geophysical analysis.

4.2 Bedrock Characterization

Williams et al., (1999) has published the only known site-specific compressional velocity (V_p) values for bedrock at Seward Park. Therefore, I used an empirical equation for weak and unconsolidated sandstones to convert uniaxial compressive strength (UCS), measurable with field methods, to compressional velocity. I first approximated bedrock uniaxial compressive strength and weathering using field criteria proposed by the International Society of Rock Mechanics (ISRM,

1978). However, since these criteria only provide a rough estimate of bedrock strength, I combined these findings with 60 Schmidt Hammer measurements previously collected to increase precision (Rains, written communication, 2018). I used the following empirical equation for weak and unconsolidated sandstones in order to compare results (Chang et al., 2006):

1) $UCS = 1.4138 \times 10^{7} \Delta t^{-3}$

Where:

Δt = interval transit time [μs/ft], where 1 μs/ft = 3.281 μs/m

UCS = uniaxial compressive strength [MPa]

$V_p = (1/\Delta t * 10^6)$ = p-wave velocity [m/s]

This information aided in my interpretations of the modeled geophysical results by allowing me to predict what range of V_p values I might expect to observe in the Blakeley Formation.

4.3 Attitude Measurements

In order to understand the geologic structures at Seward Park, I collected thirteen attitude measurements using a Brunton compass at rock outcrops on the peninsula's shoreline. I then calculated a mean pole vector using OSXStereonet (Cardozo and Allmendinger, 2013). The measurements were taken in three primary locations I have designated as the South Andrews Bay Outcrop, Kingfisher Point Outcrop, and Southeastern Outcrop respectively (Figure 9).

4.4 Test Pits

I completed ten hand-dug test pits in an attempt to validate the location of the unconformity as mapped by Troost et al., (2005). Each pit was approximately 2-3 feet deep but varied depending on regolith thickness at each specific location. I recorded GPS locations of each pit in order to conduct accurate spatial analysis out of the field. Test pit information was used in combination with Troost et al.'s (2005) mapping of the unconformity to position the survey transects for an effective geophysical analysis (Figure 10).

5.0 Electromagnetic (EM) Survey Methods

5.1 EM Surveying

Electromagnetic (EM) survey methods measure the response of the ground to the propagation of incident alternating electromagnetic waves (Reynolds, 1997). EM wave frequencies range from <10 Hz – 10^{16} Hz; however, for geophysical applications, frequencies of less than a few thousand hertz are typically used (Reynolds, 1997). A transmitter generates a primary EM field that propagates above and below ground. When EM waves travel through the ground, they are modified relative to that which travels through air generating a secondary EM field that is detected by a receiver (Figure 11). The overall response measured by the receiver is the combined effect of both the primary and secondary fields (convolution) (Reynolds, 1997). Therefore, the measured response will differ from the unmodulated primary field, and the degree in which they differ imparts information about the geometry, size, and electrical properties of any sub-surface conductor (Reynolds, 1997). There are two physical properties relevant to EM methods for geophysical applications. These include conductivity (σ), the inverse of electrical resistivity (ρ), and the dielectric constant (ε). All materials, including soil and rock, have an intrinsic resistivity that is a ratio between the current density in the material to the electric field that causes the flow of the current (Griffin, 1995). In other words, it is a measure of a materials resistance to the flow of electricity. Factors that affect resistivity in soil or rock include porosity, water content, composition (clay and metal content), salinity of the pore water, and grain size distribution (Griffin, 1995). The dielectric constant is a dimensionless property related to how a material reacts to a steady-state electric field where a potential exists, but no charge is flowing (Griffin, 1995). Heterogeneity of these factors is therefore measurable using EM methods allowing us to detect changes in composition of the subsurface.

5.2 Ground Penetrating Radar

Ground Penetrating Radar (GPR) is a common electromagnetic method used in both engineering and geological applications. GPR antenna frequencies determine the resolution and depth of investigation. A higher frequency antenna allows for greater resolution while increasing EM wave attenuation. For geological applications, such as fault delineation, soil stratigraphy mapping, and mineral exploration, depth of investigation is typically more important than very fine resolution (Reynolds, 1997). Antennae with frequencies less than or equal to 500 MHz are typically used because this allows for a survey depth of up to 30 meters in ideal conditions (Reynolds, 1997). Every GPR system includes a signal generator, transmitting antenna, receiving antenna, and

computer (a control unit) that stores the data for post-processing (Figure 12). The time it takes a radiowave to travel from the transmitter to the receiver (two-way travel time) is usually on the order of nanoseconds (Reynolds, 1997). As a GPR system is moved laterally, individual scan signals are displayed as a function of their two-way travel time in the form of a two-dimensional radargram (Figure 12). The two-way travel time is replaced by a depth scale once radiowave velocity is resolved in post-processing. However, depth can be approximated in the field if some geological information is known:

2) $V_m = c/\sqrt{\varepsilon_r}$

Where:

c = speed of light in a vacuum [m/ns]

ε_r = dielectric constant [dimensionless]

V_m = radiowave velocity [m/ns]

GPR surveys are often limited by highly conductive materials such as water-saturated clay and seawater that either absorb or reflect radiowaves to an extent that they are opaque (Reynolds, 1997). This is why the geologic setting of a survey location should be investigated prior to GPR surveying. Furthermore, successful interpretation of a GPR radargram is dependent on the strength of reflective signals produced in the subsurface. The following equation is applicable to normal incidence on a planar surface:

3) $R = \frac{\sqrt{\varepsilon_2}-\sqrt{\varepsilon_1}}{\sqrt{\varepsilon_2}+\sqrt{\varepsilon_1}}$

Where:

ε_1 = dielectric constant of layer 1 [dimensionless]

ε_2 = dielectric constant of layer 2 [dimensionless]

R = amplitude reflection coefficient [dimensionless]

Greater reflection coefficients are associated with a greater heterogeneity in dielectric constants between adjacent geologic layers. Values of the amplitude reflection coefficient range from -1 to 1 (Reynolds, 1997).

5.3 Data Collection

This project utilized a MALÅ GX GPR instrument with a shielded 80 MHz antenna (Figure 13). This low-frequency antenna was applied in order to study the subsurface at a depth of 10-20 meters. On October 26, 2017, under the supervision of Ray Cakir, I conducted a GPR survey along the western edge of the park (transect A) during sunny 60^{o}F weather and dry ground conditions. The GPR transect was 149 meters in length and ran near-perpendicular to the expected contact between Vashon till and Blakeley Formation (Figure 10). The GPR scans were annotated near any points of interest (e.g. Kingfisher Point Outcrop). The GPR was dragged at a rate of (approximately) 1 meter/second. This spatial sampling rate was determined by estimating the dielectric constant of the Blakeley Formation using an analog (wet sandstone = 6) (Figure 14). This translates to an electromagnetic wave speed of approximately 115 mm/ns. This value was inputted into the MÅLA system. Scan locations were tracked by a GPS unit. In instances where GPS signal was lost, a survey wheel attached to the back of the GPR unit was used to track the scan location. All of the data collected was transferred from the GPR instrument to a 16 GB flash drive in 32-bit RD7 format for data processing. Please refer to appendix C for additional information regarding data collection settings.

5.4 Data Processing

I processed GPR data (radargrams) using *GPR-Slice* (Goodman, 2009). Several data filters were used to enhance the reflective signals and obtain a corrected (depth) y-axis (Figure 15). A 0-ns offset was applied in order to mark the correct location at which the EM wave first contacts the ground. Next, I ran a background filter, which removes the average scan frequency from each individual scan within a radargram (Goodman, 2009). This allowed me to remove any ringing in the data. Ringing is noise that is recorded throughout the entirety of a radargram (Goodman, 2009). An automatic gain control (AGC) filter is used to strengthen signals found at greater depth, while reducing the amplitude of shallow reflections in order to increase the depth of investigation (Goodman, 2009). This filter first averages the signal within each scan over a given time window. Then, the data point at the center of the window is amplified or attenuated by the ratio of the desired output value to the average signal amplitude (Goodman, 2009). A bandpass filter was also used to remove all signal frequencies outside a desired range. This is critical because often electromagnetic frequencies from devices other than the GPR unit itself (cellphones, powerlines, etc.) are recorded by the receiving antenna (Goodman, 2009). In order to smooth the image, and therefore remove any

last bit of noise, I used a boxcar filter that averages the recorded signal within a given time-distance window. Finally, migration was used to determine the appropriate wave velocity and obtain the correct depth scale along the radargram's y-axis. For greater detail, please refer to appendix A.

6.0 Seismic Survey Methods

6.1 Seismic Surveying

A seismic wave is any mechanical vibration that results from a change in stress state induced by a physical disturbance (Griffin, 1995). Therefore, a seismic wave will travel in any direction that supports displacement. Body waves exist in both longitudinal (p) and transverse (s) forms. P-waves, or compressional waves, oscillate in a direction parallel to wave propagation (Figure 16). S-waves, or shear waves, oscillate in a direction orthogonal to wave propagation (Figure 16). Compressional velocities (V_p) are typically faster than shear velocities (V_s) (Mussett and Khan, 2000). The practice of measuring V_p and V_s is essential for geophysical research as it can be used to extract the elastic properties of soil and rock:

4) $V_p = \sqrt{\frac{\frac{4}{3}\mu + K}{\rho}}$

5) $V_s = \sqrt{\frac{\mu}{\rho}}$

Where:

μ = shear modulus [MPa]

K = bulk modulus [MPa}

ρ = bulk density [kg/m^3]

All Earth materials are comprised of up to three phases: gas, liquid, and solid (Coduto, 1999). However, because shear waves do not propagate through fluids, V_s is not directly influenced by pore fluid pressure and is a more direct representation of the soil skeleton (Reynolds, 1997). V_p and V_s values can be directly used to help identify soils and rock (Figure 17). Additionally, by comparing V_p and V_s information, porosity, fluid saturation, and many other parameters can be calculated with little additional effort (Reynolds, 1997).

6.2 Seismic Refraction

Seismic refraction is a geophysical method that utilizes p-wave travel times to gain insight. In order to understand this method, it is useful to think of a seismic wave front as a ray (Figure 18). In a homogenous medium, a seismic ray will travel in a straight line as its velocity remains constant.

However, when a seismic ray encounters a heterogeneous interface at an angle, the change in the elastic properties results in refraction (Griffin, 1995). This process is mathematically defined by Snell's Law, which can be modified for this application:

$$\textbf{6)}\quad \frac{sini_c}{v_1} = \frac{sin90}{v_2}$$

Where:

i_c = critical entry angle

v_1 = p-wave velocity of layer 1 (m/s)

v_2 = p-wave velocity of layer 2 (m/s)

Assuming a horizontal interface, there is a critical entry angle (i_c) at which the ray is refracted perpendicular to vertical causing the ray to travel directly along the interface (Figure 19). This critical angle is a function of compressional velocity on either side of the interface (Mussett and Khan, 2000). As the wave front travels just below the interface, a disturbance matches it just above the interface. However, the wavelets located above the interface generally travel at a slower velocity generating head waves, or rays that refract back to the surface at the critical angle (Figure 19). This phenomenon can be observed by measuring the time of first arrivals along a seismic array. At short distances from the induced shot point, p-waves that travel just below the ground surface (direct waves), are first to be recorded. However, after what is defined as the cross-over distance, the refracted rays arrive first. This results in a change in slope on a travel time versus distance curve produced from the recorded data (Figures 20). Since velocity is the derivative of position with respect to time, this represents a change in velocity. From this relationship, we can mathematically extract information about the subsurface.

6.3 Multichannel Analysis of Surface Waves (MASW)

In near-surface seismic surveys, when a compressional wave source is used, more than 2/3 of the total seismic energy is imparted to the in-plane surface waves known as Rayleigh waves (Park et al., 1999). In body-wave analyses, surface waves are considered noise. However, dispersion of Rayleigh waves can be used to determine the elastic properties of near-surface materials. Multichannel analysis of surface waves (MASW) is an active source seismic method that relies on the analysis of Rayleigh waves from multiple channels as a proxy for shear-wave velocity (V_s)

(Park et al., 1999). A surface wave has a different group or phase velocity (V_g or V_ϕ) at different frequency (f) (Park et al., 1999). This is the dispersion relationship. The construction of a V_s profile through the analysis of the fundamental-mode of Rayleigh waves is the most commonly used application of Rayleigh wave dispersion (Park et al., 1999). Phase velocity (velocity calculated at each frequency) is related to V_s through the dispersion relation. This characteristic, termed wave dispersion, results in a different wavelength (λ_f) for each frequency propagated (Park et al., 1999). As most earth materials have a Poisson's ratio of 0.25-0.48, the empirical approximation of Rayleigh wave velocities (V_ϕ) as shear-wave velocity (V_s) has less than a 10% error (Griffin, 1995):

Dispersion Relation	Where:
7) $\omega^2 = {V_\phi}^2 \kappa^2$	$\omega = 2\pi f$ = angular frequency, where f [Hz]
8) $V_\phi = \omega/\kappa$	V_ϕ = phase velocity [m/s]
Wave Speed Relationship	$\kappa = 1/\lambda$ = wavenumber [m^{-1}]
9) $V_s = 1.1V_\phi$	V_s = s-wave velocity [m/s]

Depth of investigation is dependent on the wavelength of a given seismic wave. Lower frequencies (longer wavelengths) can penetrate the subsurface at greater depths while high frequencies provide better resolution near the surface. The general rule of thumb is that the greatest depth that V_s can be reasonably calculated is half the longest wavelength measured (Park et al., 1999). MASW is a powerful analysis technique because it utilizes all Rayleigh wave frequencies and their associated phase velocities in order to estimate the distribution of s-wave velocity in the subsurface (Griffin, 1995).

6.4 Data Collection

I placed two geophone arrays running roughly N-S along the western and eastern edges of the park. These arrays collected the data for both MASW and refraction analysis. These transects are designated as transect A and transect B respectively (Figure 10). To see data collection details please refer to appendix C.

6.4.1 West Seward Park (Transect A)

Transect A was collected on December 7, 2017 under ideal conditions. We recorded active source in-plane compressional wave and surface wave data using 48 4.5 Hz vertical geophones with a 3-meter spacing interval (Figure 21). This resulted in an array 141 m in length. We generated a seismic source using a 16 lb. sledgehammer shot. The data were received by two 24-channel seismographs (GEODE), manufactured by Geometrics Inc. Five to twelve stacks were performed at each shot location. The seismograph was set to a 0.125-millisecond time interval sampling rate.

6.4.2 East Seward Park (Transect B)

Transect B was collected on April 26, 2018 under ideal conditions. We recorded active source in-plane compressional-wave and surface wave data using 96 4.5 Hz vertical geophones with a 2-meter spacing interval (Figure 21). This resulted in an array 190 m in length. We generated an induced seismic source using a 16 lb. sledgehammer shot. The data were received by four 24-channel seismographs (GEODE), manufactured by Geometrics Inc. Five to fifteen stacks were performed at each shot location. The seismograph was set to a 0.125-millisecond time interval sampling rate.

6.4.3 Collection Decisions

The number of stacks performed at each shot location was dependent on the amount of noise observed while in the field. Increasing the stack number resulted in a higher signal-to-noise ratio. The 0.125-millisecond sampling rate was selected in order to allow for the observation of seismic waves with a frequency of 4000 Hz (Nyquist) or less. The 4.5 Hz geophones limited our observed range to <4.5 Hz. However, body waves at higher frequencies are obscured by local noise at far offsets (Ray Cakir, personal communication, 2018). Overall, our geophones were chosen to best record for both MASW and refraction surveying.

6.5 Refraction Data Processing

Refraction data analysis was performed in the SeisImager/2D software package (Geometrics Inc., 2009). This software allows the user to process, interpret, and model two-dimensional V_p profiles from seismic refraction data. The first step of the analysis was to pick the p-wave arrivals (Figure 22). This was done over 48-channels for transect A and 96-channels for transect B. This process was performed for each shot gather in order to record p-wave first breaks along the array at every shot location. A time-distance plot was then generated that compiled these selections into one graph

(Figure 23). Finally, the time-term inversion method was used to estimate a two-dimensional V_p model (distance-depth image). Time-term inversion is a simple, but robust process that inverts travel times to obtain compressional velocity for theoretical V_p layering (Geometrics Inc., 2009). Different layers are selected where there is a break in slope (Figure 23). Time-term inversion typically is capable of identifying the first two to three transitions in compressional velocity (Mussett and Khan, 2000). This was followed by seismic tomography (an inversion process), which compares the modeled and observed travel times. 10-20 iterations were run until I produced a best fit model (RMSE<3).

6.6 MASW Data Processing

MASW data processing was performed in the SeisImager/SW software package (Geometrics Inc., 2009). This software allows the user to process, interpret, and model two-dimensional V_s profiles from surface wave data. For one-dimensional MASW analysis, a singular shot gather is used to generate a frequency-phase velocity dispersion image. The dispersion curve is selected by observing the image for frequencies that display the highest amplitude on the fundamental mode and higher modes. This follows with picking the dispersion curve on the fundamental mode portion of the image and converting the picked curve to a shear-wave velocity model. Finally, tomography, a process performed by the computer constructs a one-dimensional velocity model of the subsurface by iterating until the theoretical (calculated) dispersion curve is as close as possible to the observed curve (RMSE <3). See figure 24 for more information regarding these processing steps. In order to obtain a two-dimensional model, data from all shot gathers along the array are processed. In addition to the previous steps, common mid-point cross-correlation (CMPCC) is used (Geometrics Inc., 2009). CMPCC is a method developed by Geometrics that is used to improve the data signal and determine where along the array data results are most reliable (Figure 25).

7.0 Results

7.1 Bedrock Observations

At Seward Park, the Blakeley Formation was primarily composed of medium-coarse grained sandstone with gravel. These sandstone sequences were very thick (>10m) and had a red-orange hue. There were also some intermittent sequences of siltstone and conglomerate. Within the conglomerate sequences, the clasts were subangular and dark brown to black in color. Following the ISRM (1978) field manual for field approximation of rock strength, I was able to classify the

outcropping Blakeley Formation as "R2 Weak Rock". Through empirical study, the ISRM R2 designation is associated with a compressive strength ranging from 0-25 MPa (Figure 26). The Schmidt hammer data provided a mean compressive strength value of 15 MPa (Rains, written communication, 2018). I also evaluated the formation's general state of weathering to be slightly to moderately weathered (Figure 26). The calculated results from the empirical equation allowed me to determine a potential range of bedrock V_p values:

UCS	1 MPA	12.5 MPA	15.0 MPA (RAINS, 2018)	25 MPA
V_P	~ 1300 m/s	~ 2900 m/s	~3100 m/s	~ 3700 m/s

These calculations confirmed that the Blakeley Formation should have a V_p that is greater than Vashon till (1000-1800 m/s) (Savage et al., 2000). However, there is some noticeable overlap on the weaker end of the UCS range. I note that the value of 1833 m/s published by Williams et al., (1999) falls within the calculated range. From my work, I was also able to determine that the attitude of the Blakeley Formation within Seward Park is fairly consistent and that the mean bedding attitude is S55W, 60N (Figure 27).

7.2 Test Pit Observations

The test pits helped me refine the placement of my survey locations. At test pit 1 and 2, material observed included 1-2 ft. of colluvium underlain by weathered bedrock (Figure 28). At test pits 3 and 4, I observed colluvium only. At test pits 5-7 I observed diamict material consisting of fines and clasts of varying size and composition throughout the entire depth of the pit. Test pit 8 was dug into the side of a slope and consisted of a very thin veneer of colluvium over bedrock. Test pit 9 was located at the base of a slope. Material within this pit comprised 0.5 ft. of fines underlain by sand. Test pit 10 once again consisted of diamict material. I also observed several locations where till or bedrock was directly observable at the surface. On the western edge of Seward Park, near the mapped contact, bedrock and till were observed along the shoreline in close proximity. This is where I decided to place transect A (Figure 10). Transect B was placed near test pit 8 on the southern end and ran to where I knew till was located on the surface (Figure 10). The general location of the contact as mapped by Troost et al., (2005) was confirmed.

7.3 West Seward Park Results

The final two-dimensional V_p model depicts a relatively uniform subsurface where p-wave velocities gradually increase with depth (Figure 29). The model's V_p values range from 547 m/s at the surface to 2562 m/s at 50 m depth. There are three primary V_p groups found throughout the modeled profile. Group 1, near the surface, has a V_p that ranges from 547-771 m/s and is displayed as pink or red. Group 2 ranges from 772-1600 m/s and is displayed as yellow. Group 3, the fastest V_p group, contains p-wave velocities ranging from 1600-2600 m/s. From 60-100 meters along the profile, the velocity gradation varies slightly. At this location, group 3 velocities are observed from the base of the cross-section all the way up to 10 m depth (Figure 29). In contrast, from 0-60 m, group 1 depresses the velocity profile. The fastest velocities observed throughout the entire modeled profile can be observed 35-50 m along the x-axis at the maximum depth of 30 m.

GROUP	P-WAVE VELOCITY, V_P [M/S]
1 [PINK/RED]	547 – 771
2 [YELLOW]	900 – 1600
3 [GREEN]	1600 – 2600

The two-dimensional V_s model depicts an abrupt change in the s-wave velocity profile at 20-25 m along the profile (Figure 29). This is in contrast to the V_p model where the same general variation in velocity occurs throughout the modeled profiles length. The modeled V_s values range from 211-544 m/s. There are two primary V_s groups observed along the profile. Group 1 is located along the surface as well as at depth on the southern end of the transect (Figure 29). The V_s in this package ranges from 211-325 m/s. Group 2 V_s values range from 326-544 m/s. This group is located along the bottom of the profile from 25-140 m along the x-axis. The fastest velocities in the profile are found at 30 m depth at 75-100 m along the x-axis.

GROUP	S-WAVE VELOCITY, V_S [M/S]
1 [PINK/RED/ORANGE]	211 – 325
2 [YELLOW/GREEN]	326 – 544

The two-dimensional V_p/V_s model depicts a subsurface dominated by two primary groups with a third group which overlays them at the surface (Figure 29). Near the surface, the compressional and

shear velocities were nearly uniform resulting in ratios of 1-3. Group 1 represents this phenomenon and is symbolized by pink and red on the color scale. Group 2 represents ratios of 4-6. This group is located at depth at distances of 65-115 along the x-axis (Figure 29). On the southern end, near the start of the transect (x = 0 m), the modeled profile compressional velocities were much greater than shear velocities resulting in ratios ranging from 6-12. This velocity range, designated group 3, gradually decreases in depth as distance along the transect increases.

GROUP	V_P/V_S RATIO
1 [PINK/RED]	1 – 3
2 [YELLOW]	4 – 6
3 [GREEN/BLUE]	6 – 12

The GPR radargram was 140 meters in length (Figure 30). Several parabolic features as well as a few reflective signals are visible. The parabolic signatures are located at a depth ranging from 3-9 meters deep. These features extend throughout the entire length of the transect. The radar pulse appears to completely attenuate by a depth of 18 meters. From x=0 to x=40 meters, a few reflective signals appear to dip toward the north at a shallow angle. At x=45 to x=140 meters, a rather persistent reflector dips toward the south (Figure 30). A second reflector appears to splay off and dips at a greater angle. However, none of these reflectors dip at an angle greater than 15 degrees. No other key reflective signatures were observed in the GPR radargram.

7.4 East Seward Park Results

The two-dimensional V_p model depicts an abrupt transition in compressional velocity near the middle of the profile (Figure 31). The modeled V_p values range from 1096-3011 m/s. There are three primary V_p groups within the profile. Group 1 includes velocities ranging from 1096-1947 m/s and is displayed as pink, red, and yellow (Figure 31). Group 1 velocities appear to cover the first 10 meters in depth throughout the entire length of the profile. Group 2 velocities range from 1948-2799 m/s and are displayed in shades of yellow and green. This velocity group is approximately 40 m thick on the northern end of the profile and pinches out to thickness of 10 m to the south (Figure 31). The third and final velocity group (dark green) represents V_p values ranging from 2800-3011 m/s. This group forms the bottom of the profile. In the south, Group 3 velocities reach a shallow

depth of 10 m (Figure 31). This is in stark contrast to the northern end where Group 3 velocities are visible at 40 m depth.

GROUP	P-WAVE VELOCITY, V_P [M/S]
1 [PINK/RED/YELLOW]	1096 – 1947
2 [YELLOW / GREEN]	1948 – 2799
3 [DARK GREEN]	2800 – 3011

The two-dimensional V_s model also depicts a transition in velocity from south to north (Figure 31). The modeled V_s values range from 279-1129 m/s. Three primary V_s groups can be identified. Group 1 (red/orange) includes velocities ranging from 279-579 m/s. The first velocity group forms a veneer along the surface. It reaches a depth of 20 m in the north. From x=90 to x=190, group 1 velocities are bound to the top 5 meters of the subsurface (Figure 31). Group 2 velocities (green) range from 580-979 m/s. At x=90 to x=190, group 2 velocities are found at a shallow 5 m depth. In the middle of the image, x=90 to x=120, there is a sharp depression where group 2 velocities reach a depth of 75 meters. North of this location, group 2 velocities are observed at a greater depth in comparison to the south end of the profile. Group 3 velocities range from 980-1129 m/s and are represented in blue on the color scale. This velocity group maintains a depth of 50 meters throughout most of the profile. However, at x=120, group 3 velocities are observed as shallow as 15 meters (Figure 31).

GROUP	S-WAVE VELOCITY, V_S [M/S]
1 [RED/ORANGE]	279 – 579
2 [GREEN]	580 – 979
3 [BLUE]	980 – 1129

The two-dimensional V_p/V_s model depicts a complex distribution of ratios in the subsurface. Group 1 ratios ranging from 1.9 to 3 are found primarily along the surface. However, from x=140 to x=190 these ratios reach a dept of approximately 10 meters (Figure 31). Group 2 ratios ranging from 3 to 4.1 are found along the entire bottom of the profile. Small variations in these values can be observed (Figure 31). Group 3 ratios ranging from 4.1 to 6.8 are primarily observed at a depth of 10-25 meters from x=0 to x=50.

GROUP	V_P/V_S RATIO
1 [PINK/RED]	1 – 3
2 [YELLOW]	4 – 6
3 [GREEN/BLUE]	6 – 12

8.0 Discussion

8.1 Survey Limitations

The seismic data provided a first order representation of the subsurface while GPR data allowed me to refine my interpretations of shallow layers (approximately 0-15m). Unfortunately, GPR data were not collected at the eastern survey location. It is likely that the geology along these transects is more complicated than what is presented in this section of the report. However, the geophysical methods still provide important information for understanding the subsurface geometry along the geologic contact. It is important to note that the geophysical techniques used to interpret the geometry of the unconformity at depth are dependent on ground truthing using control points. If these boundary conditions are not available, geophysical analyses are no longer reliable. Additionally, geophysics is used to measure the physical properties of materials and provide parameters that we cannot directly observe. Several geological configurations could potentially reproduce the measurements observed in this study. I will propose some of these plausible scenarios.

8.2 Interpreted Geologic Units

I have interpreted three geologic units using information obtained from the geophysical surveys coupled with my observations at the surface. It is likely that the subsurface has a more complex geology than what is presented. Nonetheless, these generalizations are useful in discussing the potential geometry of the unconformity in the subsurface. Additional work will be required to refine these interpretations.

8.2.1 Unit 1 – Unconsolidated Holocene Sediments

The first interpreted unit is generalized as unconsolidated Holocene sediments (H). This unit was interpreted to exist near the surface at transect A (~upper 4-5m) (Figure 32). Compressional velocities for this unit range from approximately 541-777 m/s. Shear velocities for this unit range from approximately 211-320 m/s. These velocities are generally associated with unconsolidated

Earth materials such as scree, vegetal soil, and dry sand (Coussy, 1987). These low velocities are not common in transect B and where they are found they are isolated. Therefore, I have not interpreted this same unit to be located within transect B (Figure 33). From the calculated V_p/V_s profile, I was able to infer that this material was likely dry and/or impermeable. This is because the V_p/V_s ratio is often used as an indicator for pore fluid pressure (Ray Cakir, personal communication, 2018). This unit had a low ratio suggesting that there was little pore fluid pressure measured (Figure 32). At the time of data collection, I observed Lake Washington's elevation was roughly 4 meters below the ground surface. This may explain the low ratios associated with this unit. The GPR radargram recorded at transect A was also useful in interpreting this unit. Parabolic reflectors begin to appear at a depth of approximately 3 meters (Figure 30). These parabolic reflectors can be generated by large rocks, pipes, culverts, or other discrete objects (Goodman, 2009). While I cannot rule out the possibility of these objects being pipes or other man-made objects, I believe the frequency in which they are observed indicate that they are of natural origin. Large rocks are not typically associated with artificial fill that may have been placed during the original grading and construction of the path. Also, if this unit represents Holocene lake deposits, it was likely deposited by Lake Washington before the lowering of its elevation in 1916 (Chrzastowski, 1983). Therefore, the unit would contain fine-grained materials (Karlin et al., 2004). These parabolic features are expected in till, colluvium, or highly weathered bedrock where large gravels, cobbles or cores stones may be found. Therefore, the parabolic features could mark the bottom of this unit. However, if this unit represents unconsolidated colluvium, it may extend further as the parabolic signatures are not diagnostic.

8.2.2 Unit 2 - Vashon Till

Vashon till (Qvt) is described as a compact diamict of silt, sand, and subrounded to well-rounded gravel with cobbles and boulders (Troost and Booth, 2008). Compressional velocities of Vashon till typically range from 1000-1800 m/s while shear velocities range from 360-760 m/s (Savage et al., 2000). These velocity ranges can be observed along both transects. In transect A, the V_p profile is not helpful in distinguishing this layer as almost all of the subsurface displays compressional velocities faster than 1000 m/s (Figure 32). I attribute this to the influence of pore fluid pressure. Water has a V_p that ranges from 1450-1500 m/s (Coussy, 1987). While the V_p profile is not particularly helpful, the interpreted till is distinguishable in the V_s profile. From x=25 to x=140, the shear velocities fall within the range typical of till (Figure 32). These same shear velocities are not

observed from x=0 to x=25. Transect B also had velocities that would match those of till. These velocities are found from x=120 northward and are confined within a depth of 20 meters (Figures 33). The V_p/V_s profiles from both survey locations measure a ratio for this unit as ranging from about 4-7 (Figure 32). This indicates that there is slightly more pore fluid pressure than in the Holocene soils. This would be expected as this unit sits almost entirely below the water table. Furthermore, these geophysical interpretations match the location of Vashon till as mapped by Troost and Booth, (2005).

8.2.3 Unit 3 - Blakeley Formation Bedrock

I have interpreted the third unit as the Blakeley Formation (Tb). The Blakeley Formation at Seward Park has been described as interbedded medium-grained sandstone, coarse-grained sandstone, conglomerate, and minor siltstone (Troost and Booth, 2008). Generalized shear velocity values for porous and unconsolidated sandstones typically range from 800-1800 m/s while compressional velocities range from 2000-3500 m/s (Coussy, 1987). These velocities can be observed within transect B (Figures 33). A gradual decrease in velocity is also observed with decreasing depth indicating the unit is weathering and losing strength near the surface (Figures 33). These slightly lower velocity measurements near the surface match my observations of bedrock strength and weathering. However, at the western survey (transect A), shear velocities have been measured as much lower (200-300 m/s) (Figure 32). These V_s values originally appear to be a mismatch. However, site-specific data produced by Williams et al., (1999) and Wong et al., (2001) suggest that the Blakeley Formation at Seward Park could match these low velocities within a depth of 30 meters. Within the first 10 meters, Wong et al., (2001) measured V_s values as low as 228 m/s. From 10-30 meters, a slight increase in velocity (457 m/s) was observed. I suspect that these velocities occur where the Blakeley Formation has been displaced by some post-depositional event, perhaps a landslide. The Kingfisher Point Outcrop is located near transect A (Figure 9). The outcrop is characterized by a concave shape that opens toward the northwest. Additionally, bedrock bedding dips at 60^o out of the face of the outcrop (Figure 9). This may suggest that this is the location of a historic landslide and that the outcrop represents a landslide scarp. Many co-seismic landslides are thought to have occurred along Lake Washington's shoreline (Karlin et al., 2004). V_p/V_s ratios also varied between the two survey locations. The unit appears to be less porous therefore containing less pore fluid on the eastern side of Seward Park (transect B) (Figures 32 and 33). This could also be due to differences in post-depositional processes experienced by the rock at each location.

8.3 Subsurface Geometry

The data indicate that there is a lateral transition in geology from south to north as expected from the geologic map. Furthermore, from my observations and measured results, I have inferred that the bedrock elevation is much greater in the south and that the contact exists at a relatively steep angle (Figures 32 and 33). This geometry has several plausible explanations, the most plausible of which I present here. I note that the western survey location (transect B) was particularly helpful in this portion of my analysis due to the greater depth of investigation along this transect (~80 m). However, both transects provided important information. The following geologic scenarios were interpreted assuming that the assignment of geologic units in the previous section is correct.

8.3.1 Buttress Unconformity

One plausible scenario is that this subsurface geometry represents a buttress unconformity (Figure 34). Buttress unconformities occur when beds of younger material are deposited in a region of significant pre-depositional topography. The Blakeley Formation was deposited at the Oligocene-Miocene boundary approximately 23 Ma (Troost and Booth, 2008). In comparison, the Vashon glaciation occurred within the last twenty thousand years (Porter and Swanson, 1998) and older glaciations occurred in the last 1.8 Ma. There is a large gap in the geologic timescale between the deposition of the Tertiary bedrock and Quaternary deposits. It is possible that the Blakely Formation's bedding attitude was determined thousands to millions of years before the Vashon till was deposited and that Quaternary sediments were deposited adjacent to and eventually on top of the bedrock. Depending on the model and where the contact is measured, it is possible that the contact dips <60^{o} (Figure 33). The N-S trend of the transect means that the apparent dip of the Blakeley Formation bedding plane would also be more gradual than the measured true dip (=60^{o}). However, at transect A, shear velocity transition appears to be near vertical which would not be expected in this scenario (Figure 32). Another potential issue with this interpretation is the higher velocity zone north of x=100 along transect B (Figures 33). These velocities are too high to be Quaternary sediments and are in general more representative of bedrock (Savage et al., 2000; Coussy, 1987). Since the bedrock was measured to dip at 60 degrees to the northwest, it would be unlikely that the contact surface undulate in this manner. If this zone is also Blakeley Formation, this means that the bedrock would have a tight fold in the subsurface. However, it is also possible that this zone represents a different rock unit not observed.

8.3.2 Erosional Unconformity

A second hypothesis is that this contact represents an erosional unconformity (Figure 34). In this scenario, one or multiple erosive events would have removed and transported the Blakeley Formation on the northern ends of each transect before or perhaps during the deposition of the Vashon till. One possible mechanism is a pre-Pleistocene river channel. This river could have flowed west from the proto-Cascades toward the ocean (Kathy Troost, written communication, 2018). The velocity offset could therefore represent a transition between a bluff and its associated river cut terrace. The data from transect B suggest that there is at least a 20-meter drop in bedrock elevation from south to north (Figures 32 and 33). Modern day analogues suggest that such an erosional offset is possible. Reflective boundaries found in the GPR radargram also dip at low angles toward a centralized location (Figures 30). Perhaps these features mark the location of a historical topographic low such as a river channel. In addition to fluvial geomorphic processes, glacial scouring has largely impacted the local geology of the Puget Lowland (Booth et al., 2003). Glacial ice sheets moved from north to south scouring and depositing material and are responsible for many of the bluffs, troughs, and other features seen today (Booth et al., 2003). Glacial scouring during any one of seven glacial advances (Troost and Booth 2008) may have created the observed unconformity. However, an abrupt change in bedrock elevation would not be expected from this kind of erosional event. Generally, glacial erosion results in asymmetric landforms. Increased abrasion rates where the ice first makes contact against a bedrock knob results in a gradual slope where plucking of jointed bedrock on the leeward side creates steep topography (Terry Swanson, personal communication, 2017). Since this contact is on the northern side of the bedrock, I find this mechanism less likely.

8.3.3 Fault-Generated Unconformity

A third hypothesis is that this unconformity is the result of a south-side-up thrust fault within the SFZ (Figure 34). This could explain how the Tertiary bedrock is sitting at the same stratigraphic level as Vashon till. With this interpretation, the 20-meter drop in perceived bedrock elevation would be a stratigraphic offset associated with fault displacement. Data gathered along transect B supports this hypothesis. Transect B's V_s profile shows a southward dipping (30-40^o) depression in velocity. This depression runs from about x=60 to x=130 and runs through the interpreted bedrock formation (Figure 33). However, this depression ends where I have interpreted the bottom extent of the Vashon till and does not continue to the surface. It is therefore possible that this is a blind fault

that does not outcrop at the ground surface. Near a fault surface, one might expect bedrock to be more heavily fractured due to tectonic shearing in a brittle environment. This would cause a decrease in shear velocities. Decreased velocities can be observed around the observed lineament (Figure 33). The uniaxial compressive strength of the Blakeley Formation has been determined from multiple sources to be unusually low near the surface (Williams et al., 1999; Wong et al., 2011; Troost and Booth, 2008). This may be one potential explanation as to why this interpreted shear zone is rather wide (Figure 33). However, I also note that the change in shear velocity is only on the magnitude of a few hundred meters per second. One potential issue with this hypothesis is that the interpreted lineament is nowhere to be found in the data collected at transect A (Figure 32). This may be due to the limited survey depth of 30 meters, or it may be that the measured shear velocity lineament is caused by some other process.

9.0 Limitations

There are several limitations involved with this research work. As stated previously, geophysical results are non-unique, and the measured results can be generated by several geologic configurations. Until more concrete evidence is collected, the exact cause of the measured results will remain unknown. Furthermore, this project relied on sparse surface observations in order to make some key assumptions about the subsurface geology. Without a better understanding of the subsurface geology via borehole data or trenching, it is not possible to resolve many of the potential geologic mechanisms for the measured results. It is also likely that the geology of the local subsurface is more complex than what is presented in this report. Seismic methods are not capable of modeling the subsurface in extreme detail. Another limitation includes the depth of exploration. The seismic and electromagnetic methods used in this project were only capable of measuring up to a combined depth of 30 meters at transect A and 80 meters at transect B. While these are significant depths, these near-surface geophysical techniques are not the preferred method for fault investigation because material near the surface is often weathered, water saturated, and displaced, which can significantly skew interpretations. Lastly, the scope of this research work was limited due to time factors and only several potential causes of the measured results could be explored.

10.0 Recommendations for Future Work

To perform an ideal investigation, I recommend the use of a larger seismic source and implementation of seismic reflection in order to investigate to greater depths. Seismic reflection is superior to shallow geophysical methods for fault investigation and is commonplace within the oil industry as well as the geophysical research community. I also recommend extending the transect A array while also decreasing the geophone spacing for a more resolute image. A third array should be conducted in the middle of the peninsula. If the location of the unconformable contact at the crest of the park can be found, trenching could be used to determine if a fault is present and obtain the date of fault offset. Near the surface, the bedrock was of poor quality making its distinction from colluvium, till, and Holocene deposits difficult. Obtaining borehole information would prove invaluable in delineating the subsurface, especially in the shallow zone where weathering influences are greatest. This would allow for a more concrete interpretation of the seismic velocities since specific V_p and V_s values could be better matched with direct observations. A more detailed geologic map of Seward Park should also be created. This project relied on the best available geologic data at a scale of 1:12,000. However, I have found the geology to be more complex along the margins of the Bailey Peninsula. Finally, seismic methods are negatively affected by any vibrational disturbances near the recording geophones. While conducting this work, one major challenge included recording data without pedestrian induced noise. In order to minimize this complication, I recommend using traffic cones and additional survey members who can control pedestrian traffic.

11.0 Conclusions

Previous research has identified a geophysical anomaly on Mercer Island that trends in a direction roughly parallel to a mapped geologic unconformity at Seattle's Seward Park. The anomaly is also geographically located at the same latitude as the unconformity. Due to its location and general orientation, this lineament has been speculated as a strand of the SFZ. To better understand the unconformity, I performed geophysical surveys that measured the subsurface near the contact. These surveys measured the subsurface to a maximum depth of 80 meters allowing for a first-order approximation of the subsurface geometry along the contact. The data collected has identified a

clear transition of material properties consistent with the mapped unconformity and observations made while performing field work. The Vashon till, mapped on the north end of Seward Park, was observed to have V_s values of 250-500 m/s and V_p values of 1000-1700 m/s. The Tertiary bedrock, on the southern end, was observed to have V_s values as low as 229 m/s and as high as 1129 m/s. The contact also appears to be abrupt and exist at a fairly steep angle. The exact angle is difficult to resolve leaving some uncertainty and room for different interpretations. From my findings, I contend that a buttress, erosional, or fault-generated unconformity are the most plausible explanations for the measured geologic contact in Seward Park. It is also possible that some combination of the proposed mechanisms is responsible for producing this unconformity. While my findings do not provide concrete evidence supporting the unconformity to be fault-generated, neither do they refute this hypothesis. More research is required to fully diagnose the nature of this unconformity.

12.0 References Cited

Atwater, B.F. and Moore, A.L., 1992. A tsunami about 1000 years ago in Puget Sound, Washington. Science-New York then Washington- 258, pp. 1614-1614

Aspect Consulting, LLC, 2015. A Geologist's Thoughts on the Pacific Northwest Mega-Quake Story: https://www.aspectconsulting.com/blog/2015/7/27/a-geologists-thoughts-on-the-pacific-northwest-mega-quake-story (accessed 6-5-18).

Blakely, R.J., Wells, R.E., Weaver, C.S. and Johnson, S.Y., 2002. Location, structure, and seismicity of the Seattle fault zone, Washington: Evidence from aeromagnetic anomalies, geologic mapping, and seismic-reflection data. Geological Society of America Bulletin, 114(2), pp.169-177.

Blakely, R.J., Sherrod, B.L., Hughes, J.F., Anderson, M.L., Wells, R.E. and Weaver, C.S., 2009. Saddle Mountain fault deformation zone, Olympic Peninsula, Washington: Western boundary of the Seattle uplift. Geosphere, 5(2), pp.105-125.

Booth, D.B., Troost, K.G., Clague, J.J. and Waitt, R.B., 2003. The Cordilleran ice sheet. Developments in Quaternary Sciences, 1, pp.17-43.

Bourgeois, J., and S. Johnson (2001), Geologic evidence of earthquakes at the Snohomish delta, Washington, in the past 1200 yr, Bull. Seismol. Soc. Am., 113(4), 482–494.

Brink, U.T., Molzer, P.C., Fisher, M.A., Blakely, R.J., Bucknam, R.C., Parsons, T., Crosson, R.S. and Creager, K.C., 2002. Subsurface geometry and evolution of the Seattle fault zone and the Seattle basin, Washington. Bulletin of the Seismological Society of America, 92(5), pp.1737-1753.

Brocher, T. M., R. J. Blakely, and R. E. Wells (2004), Interpretation of the Seattle uplift, Washington, as a passive-roof duplex, Bull. Seismol. Soc. Am., 94, 1379–1401.

Bucknam, R. C., E. Hemphill-Haley, and E. B. Leopold (1992), Abrupt uplift within the past 1700 years at southern Puget Sound, Washington, Science, 258, 1611–1614, doi:10.1126/science.258.5088.1611.

Cardozo, N. and Allmendinger, R.W., 2013. Spherical projections with OSXStereonet. *Computers & Geosciences*, *51*, pp.193-205.

Chang, C., Zoback, M.D. and Khaksar, A., 2006. Empirical relations between rock strength and physical properties in sedimentary rocks. Journal of Petroleum Science and Engineering, 51(3-4), pp.223-237.

Chrzastowski, M.J., 1983. Historical changes to Lake Washington and route of the Lake Washington Ship Canal, King County, Washington (No. 81-1182). Geological Survey (US).

Coduto, D.P., 1999. Geotechnical engineering: principles and practices (No. Sirsi) i9780135763803).

Coussy, O., 1987. Acoustics of porous media. Editions Technip.

Daneš, Z.F., Bonno, M.M., Brau, E., Gilham, W.D., Hoffman, T.F., Johansen, D., Jones, M.H., Malfait, B., Masten, J. and Teague, G.O., 1965. Geophysical investigation of the southern Puget Sound area, Washington. Journal of Geophysical Research, 70(22), pp.5573-5580.

Earthquake Engineering Research Institute, and Washington Military Department: Emergency Management Division, 2005, Scenario for a Magnitude 6.7 Earthquake on the Seattle Fault: EERI, p. 117.

Geometrics Inc., 2009. SeisImager/SW™. software manual; version 2.2.

Geometrics Inc., 2009. SeisImager/2D™. software manual; version 3.3, 257pp.

Goodman, D., 2009. GPR-SLICE v6. 0 Manual.

Griffin, R.H., 1995. Geophysical exploration for engineering and environmental investigations. US Army Corps of Engineers.

Harding, S.T., Urban, T.C., and Barnhard, T.P., 1988, Preliminary evidence of possible Quaternary faulting in Puget Sound, Washington, from a multichannel marine seismic reflection survey, in Hays, W.W., ed., Workshop on ‘‘Evaluation of earthquake hazards and risk in the Puget Sound and Portland areas’’: U.S. Geological Survey Open-File Report 88–541, p. 178–193.

Huntley, D. J., and J. J. Clague (1996), Optical dating of tsunami-laid sands, Quat. Res., 46, 127–140.

ISRM, 1978. “Commission on Standardization of Laboratory and Field Tests: Suggested methods for the quantitative description of discontinuities in rock masses.” International Journal of Rock Mechanics, Mining Sciences and Geomechanics. Abstract Vol. 15 pp. 319-368.

Jacoby, G. C., P. L. Williams, and B. M. Buckley (1992), Tree ring correlation between prehistoric landslides and abrupt tectonic events in Seattle, Washington, Science, 258, 1621–1623.

Johnson, S.Y., Dadisman S.V., Childs J.R., and Stanley W.D., 1999, Active Tectonics of the Seattle Fault and Central Puget Sound, Washington—Implications for Earthquake Hazards: Geological Society of America Bulletin v. 111, p. 1042- 1053.

Johnson, S.Y., Potter C.J, and Armentrout J.M., 1994, Origin and Evolution of the Seattle Fault and Seattle Basin, Washington: Geology v. 22, p. 71.

Karlin, R., and S. E. Abella (1996), A history of Pacific Northwest earthquakes recorded in Holocene sediments from Lake Washington, J. Geophys. Res., 101(B3), 6137–6150, doi:10.1029/95JB01626.

Karlin, R.E., Holmes, M., Abella, S.E.B. and Sylwester, R., 2004. Holocene landslides and a 3500-year record of Pacific Northwest earthquakes from sediments in Lake Washington. GSA Bulletin, 116(1-2), pp.94-108.

Kelsey, H.M., Sherrod, B.L., Nelson, A.R. and Brocher, T.M., 2008. Earthquakes generated from bedding plane-parallel reverse faults above an active wedge thrust, Seattle fault zone. Geological Society of America Bulletin, 120(11-12), pp.1581-1597.

Lamb, A.P., Liberty, L.M., Blakely, R.J., Pratt, T.L., Sherrod, B.L. and van Wijk, K., 2012, Western limits of the Seattle fault zone and its interaction with the Olympic Peninsula, Washington: Geosphere, 8(4), pp.915-930.

Liberty, L.M. and Pratt, T.L., 2008, Structure of the eastern Seattle fault zone, Washington State: New insights from seismic reflection data: Bulletin of the Seismological Society of America, 98(4), pp.1681-1695.

Martin, M. E., and J. Bourgeois (2011), Vented sediments and tsunami deposits in the Puget Lowland, Washington - Differentiating sedimentary processes, Sedimentology, 59(2), 419–444, doi:10.1111/j.1365-3091.2011.01259.x.

McCaffrey, R., Qamar, A.I., King, R.W., Wells, R.E., Khazaradze, G., Williams, C.A., Stevens, C.W., Vollick, J.J., and Zwick, P.C., 2007, Fault locking, block rotation and crustal deformation in the Pacifi c Northwest: Geophysical Journal International, v. 169, p. 1315– 1340, doi:10.1111/j.1365-246X.2007.03371.x

Mussett, A.E. and Khan, M.A., 2000. Looking into the earth: an introduction to geological geophysics. Cambridge University Press.

Nelson, A.R., Johnson, S.Y., Kelsey, H.M., Wells, R.E., Sherrod, B.L., Pezzopane, S.K., Bradley, L.A., Koehler III, R.D. and Bucknam, R.C., 2003. Late Holocene earthquakes on the Toe Jam Hill fault, Seattle fault zone, Bainbridge Island, Washington. Geological Society of America Bulletin, 115(11), pp.1388-1403.

Park, C.B., Miller, R.D. and Xia, J., 1999. Multichannel analysis of surface waves. Geophysics, 64(3), pp.800-808.

Porter, S.C. and Swanson, T.W., 1998. Radiocarbon age constraints on rates of advance and retreat of the Puget lobe of the Cordilleran ice sheet during the last glaciation. Quaternary Research, 50(3), pp.205-213.

Pratt, T.L., Troost, K.G., Odum, J.K. and Stephenson, W.J., 2015. Kinematics of shallow backthrusts in the Seattle fault zone, Washington State. Geosphere, 11(6), pp.1948-1974.

Reynolds, J.M., 2011. An introduction to applied and environmental geophysics. John Wiley & Sons.

Savage, W.Z., Morrissey, M.M. and Baum, R.L., 2000. Geotechnical properties for landslide-prone Seattle; area glacial deposits (No. 2000-228). US Department of the Interior, US Geological Survey,.

Sherrod, B.L., Bucknam, R.C., and Leopold E.B., 2000, Holocene Relative Sea Level Changes along the Seattle Fault at Restoration Point, Washington: Quaternary Research, v. 54, p. 383-394.

Sherrod, B. and Gomberg, J., 2014. Crustal earthquake triggering by pre-historic great earthquakes on subduction zone thrusts. Journal of Geophysical Research: Solid Earth, 119(2), pp.1273-1294.

Stephenson, W.J., Frankel, A.D., Williams, R.A., Odum, J.K., and Pratt, T.L., 2007, Seismic imaging of the Seattle fault zone at West Seattle and Mercer Island, Washington: Implications for Earthquake Hazards: Seismological Research Letters, v. 78, p. 280.

Talbert P., 2017, The Geology of Seward Park: http://www.sewardpark.org/geology.html (accessed 6-8-17)

Troost K.G., Booth, D.B., Wisher A.P., Scott S.A., 2005, The Geologic Map of Seattle—A Progress Report: U.S. Geological Survey, scale 1:12000, 1 sheet

Troost K.G. and Booth D.B, 2008, Geology of Seattle and the Seattle area, Washington: Geological Society of America Reviews in Engineering Geology, v. XX. p. 1-35.

Vidale J., 2013, Seattle Hazard Identification and Vulnerability Analysis [Report]: https://www.seattle.gov/Documents/Departments/Emergency/PlansOEM/SHIVA/2014-04-23_Earthquakes(0).pdf (accessed 4-10-17).

Williams, R.A., Stephenson, W.J., Frankel, A.D. and Odum, J.K., 1999. Surface seismic measurements of near-surface P-and S-wave seismic velocities at earthquake recording stations, Seattle, Washington. Earthquake Spectra, 15(3), pp.565-584.

Wong, I.G., Stokoe, K.H., Cox, B.R., Lin, Y.C. and Menq, F.Y., 2011. Shear-wave velocity profiling of strong motion sites that recorded the 2001 Nisqually, Washington, earthquake. Earthquake Spectra, 27(1), pp.183-212.

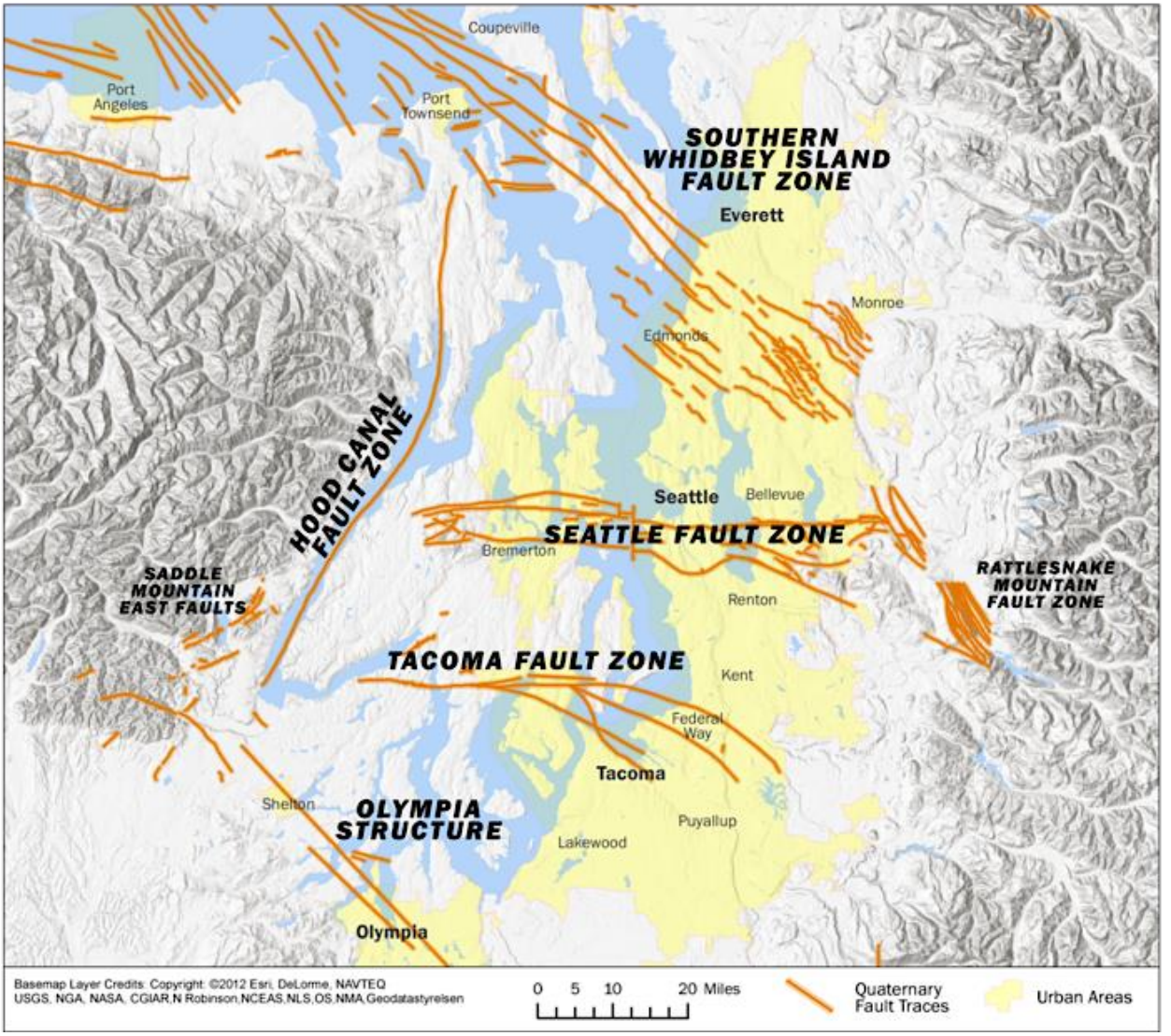

Figure 1: Regional fault systems found throughout the Puget Lowland (Aspect Consulting LLC, 2015). Interpreted Quaternary crustal faults are marked in orange. Urban areas are shaded in yellow.

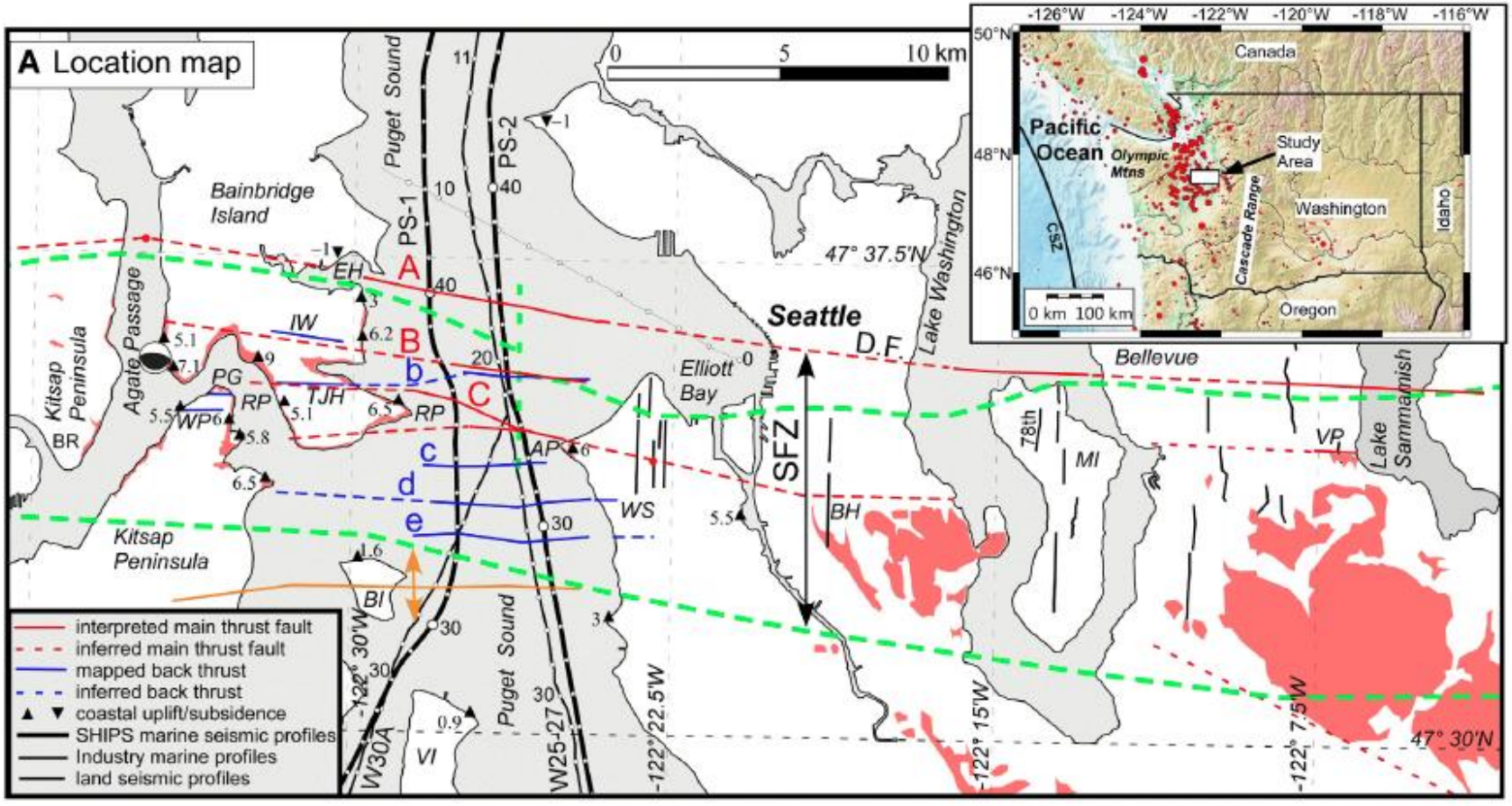

Figure 2: Depiction of the Seattle Fault Zone (Pratt et al., 2015).

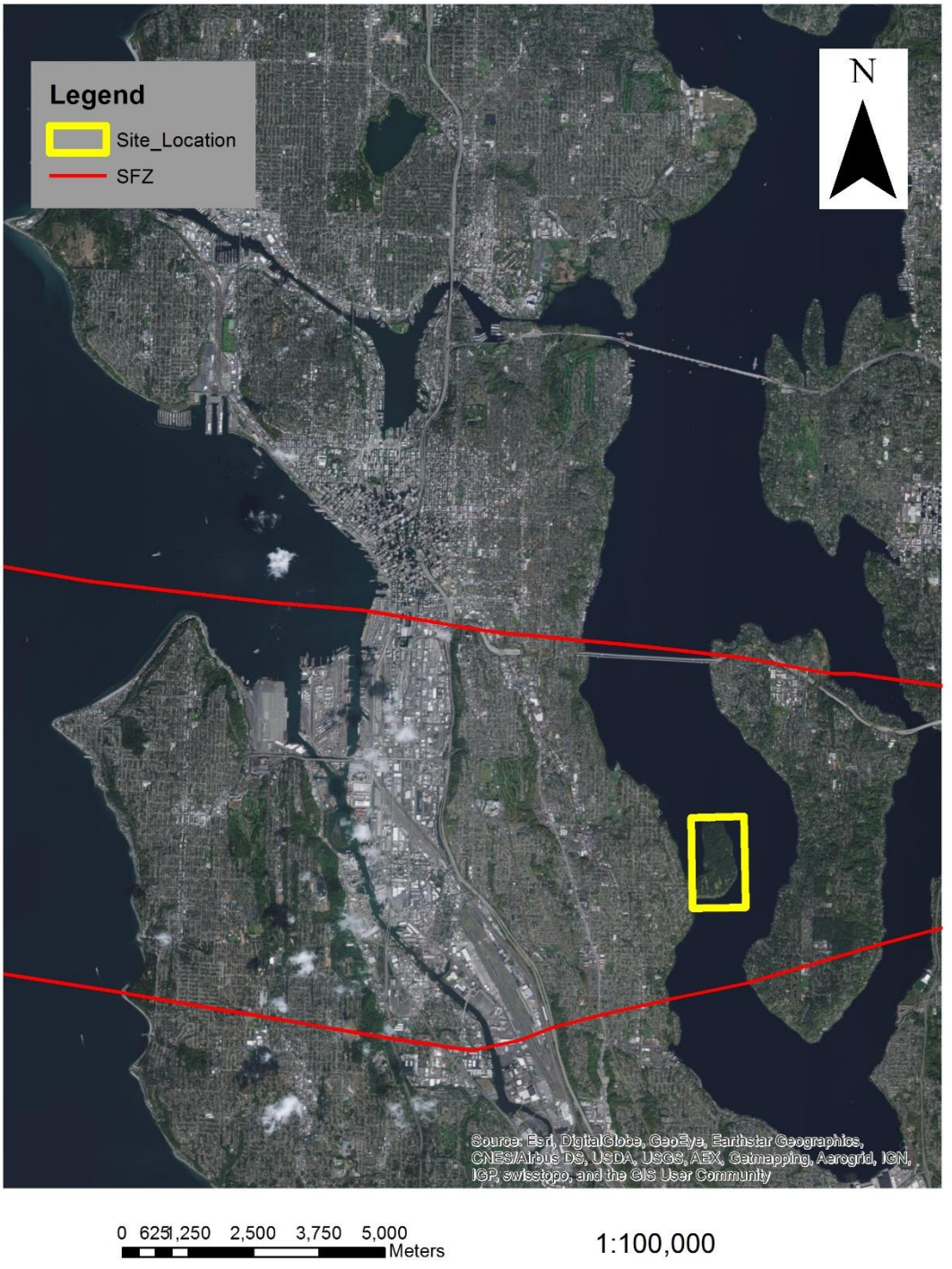

Figure 3: The Bailey Peninsula, or Seward Park (yellow rectangle) is located directly in-between two major reverse faults mapped that constitute the edges of the Seattle Fault Zone (SFZ). Fault traces from the Washington Geological Survey.

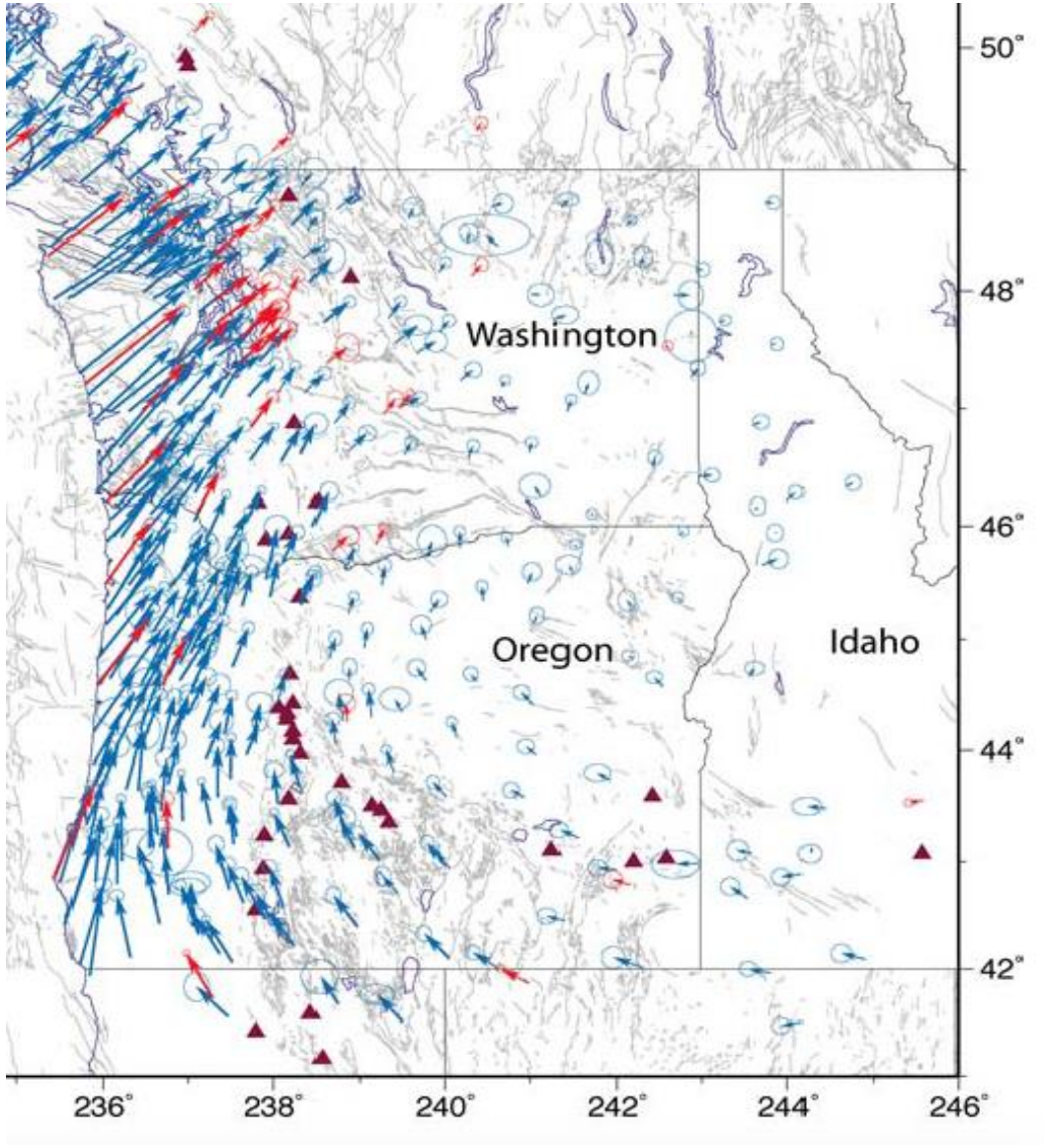

Figure 4: GPS vectors displaying the northeasterly migration of coastal Washington State relative to stable North America (McCaffery et al., 2014).

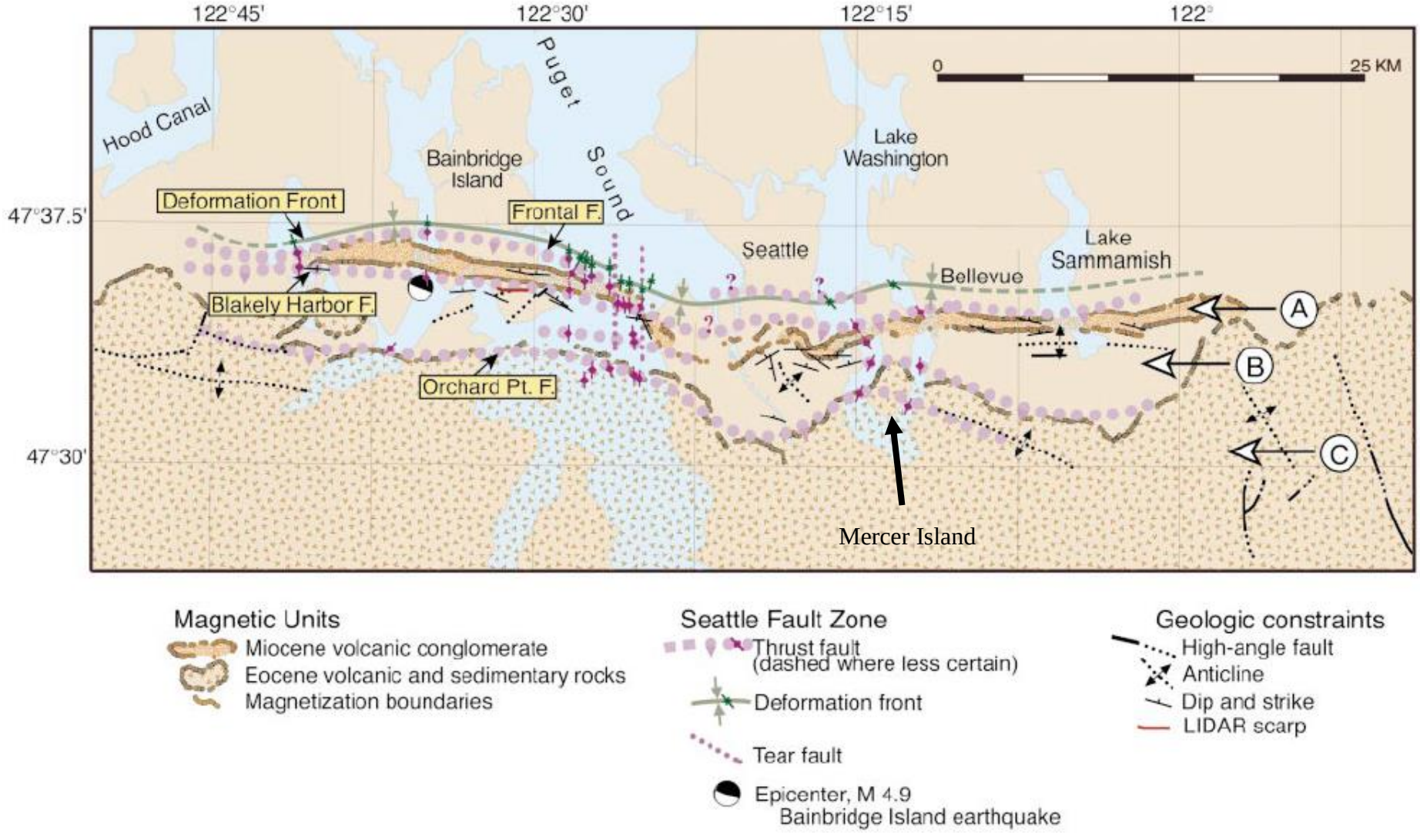

Figure 5: Map produced by Blakely et al. (2002). This study showed that a fault strand is possibly trending E-W through Mercer Island at a trajectory that would cross Seward Park.

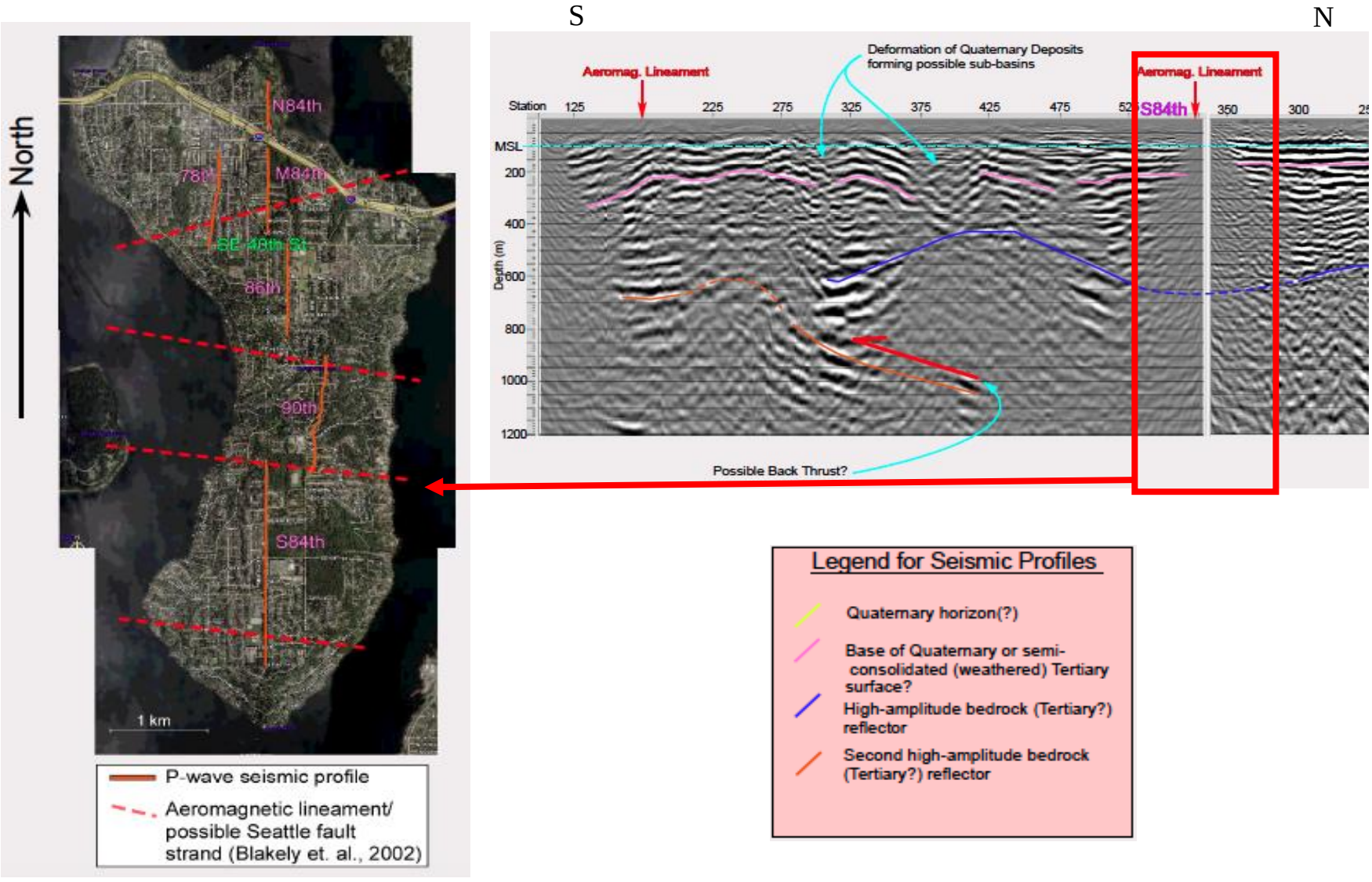

Figure 6: Pictured left is a close-up of several aeromagnetic lineaments as observed by Blakely et al., (2002). Pictured right is the result of a seismic reflection survey performed by Stephenson et al., (2007). Note the lack of reflective barriers at this location where the interpreted Quaternary stratigraphy is not observed.

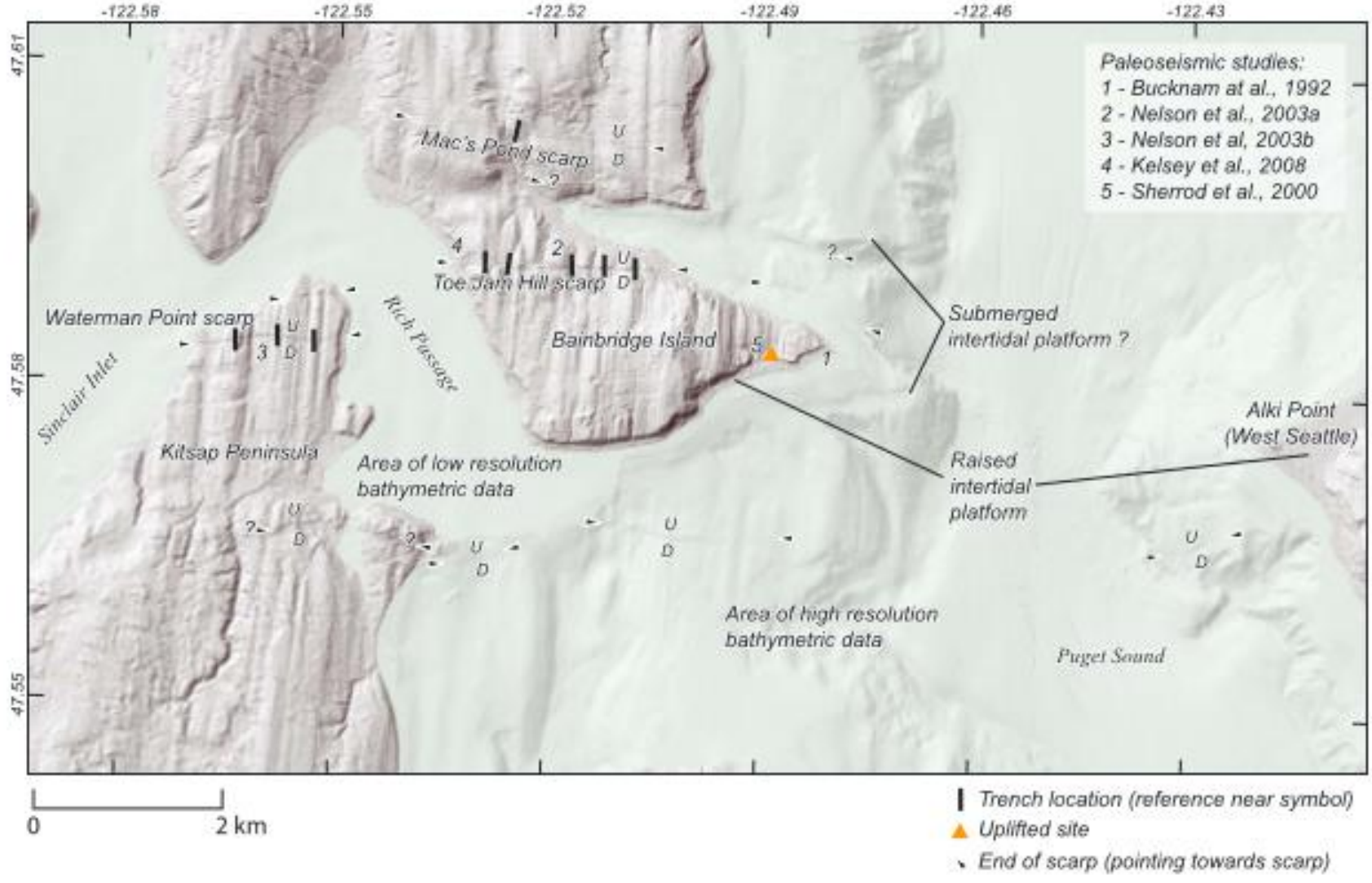

Figure 7: Shaded relief Lidar and bathymetric image of the SFZ showing the location of several paleoseismic studies as well as some key features (Sherrod and Gomberg, 2014).

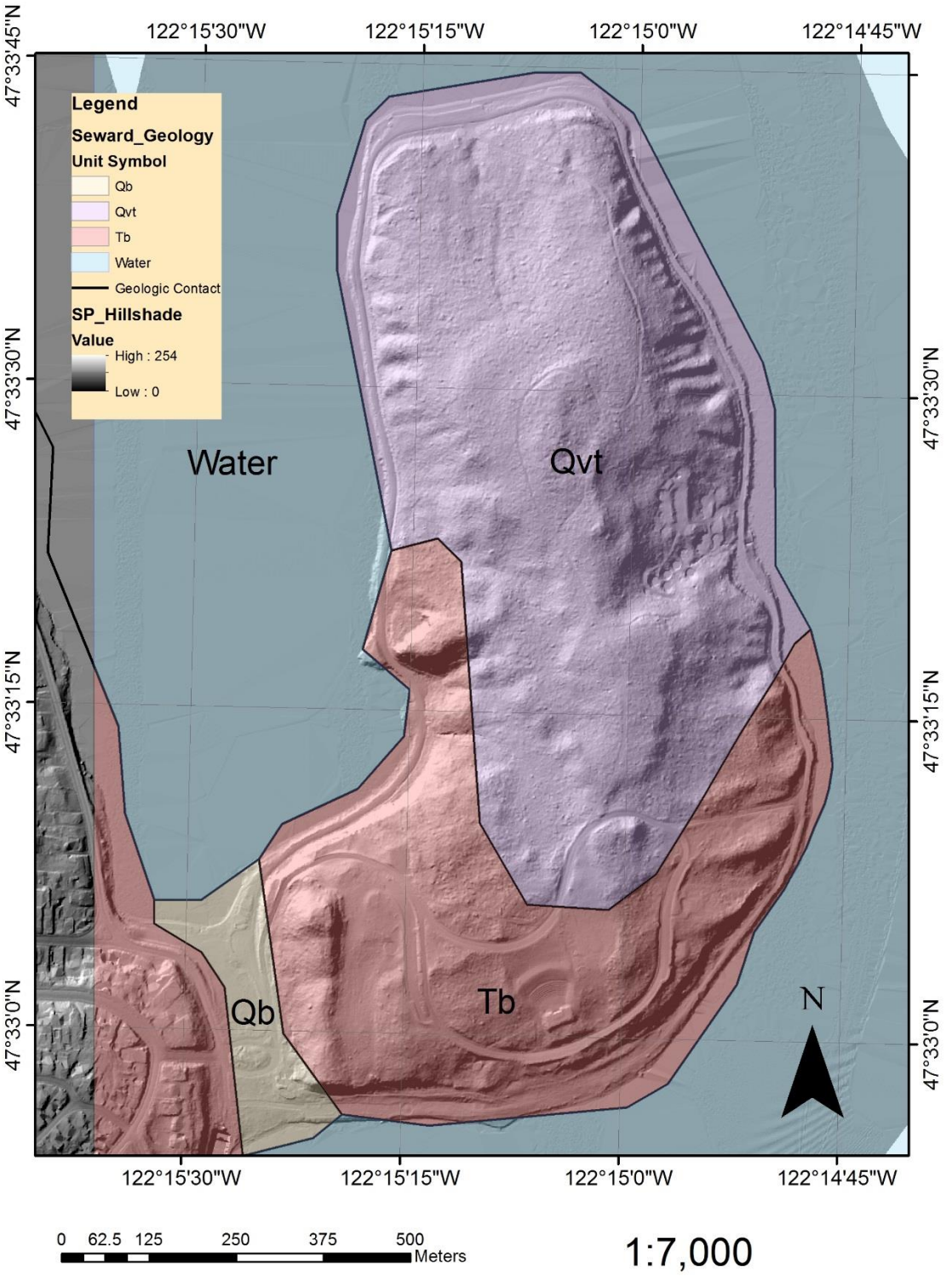

Figure 8: Seward Park geology as mapped at a 1:12,000 scale (Troost and Booth, 2005). The geology comprises Tertiary bedrock (Tb) called the Blakely Formation in the south and Vashon till (Qvt) in the north. Steep bluffs and landslides are visible along the edges of the peninsula.

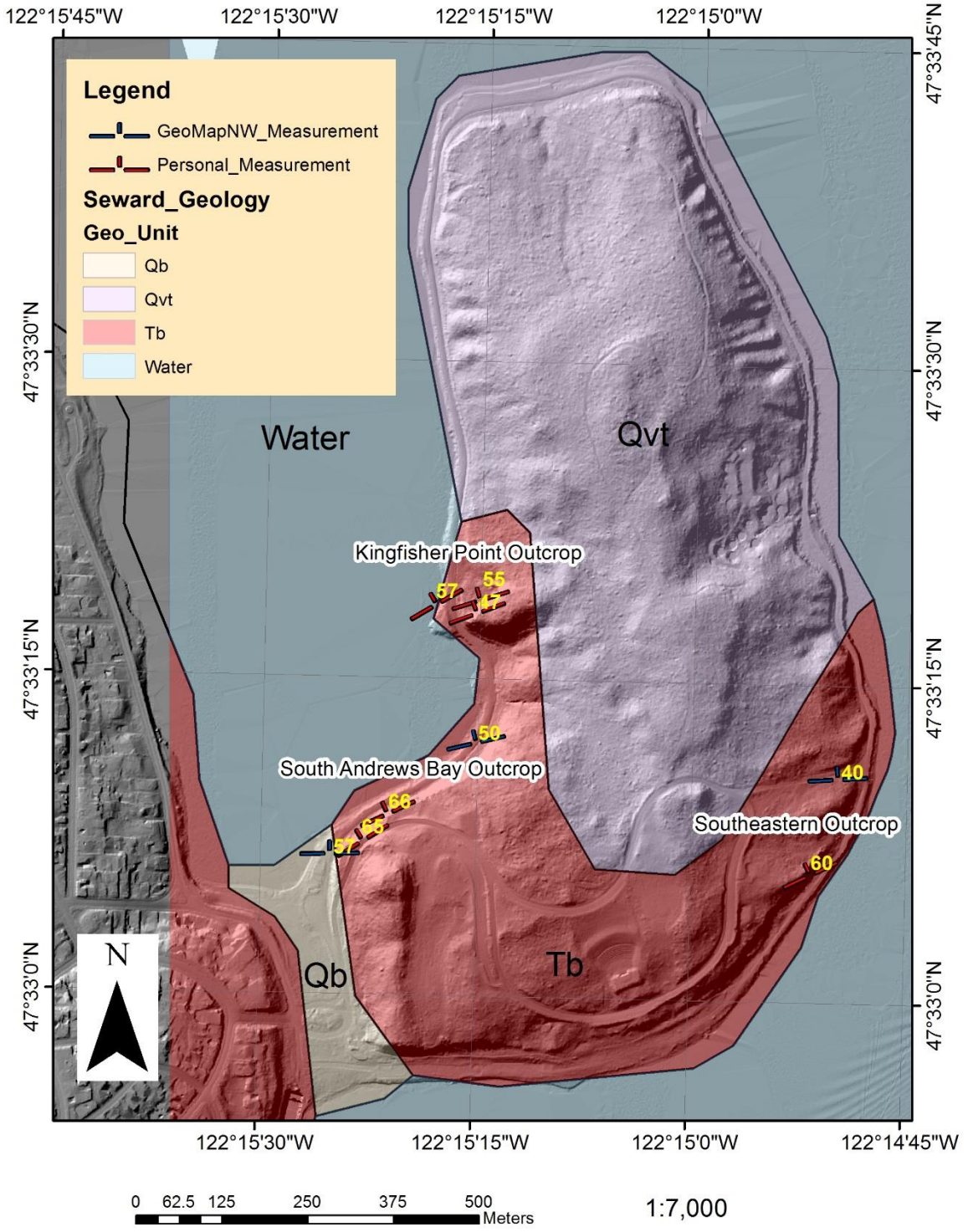

Figure 9: Location of outcrops measured in this study. A small sample of my measurements as well as those produced by GeoMapNW are shown.

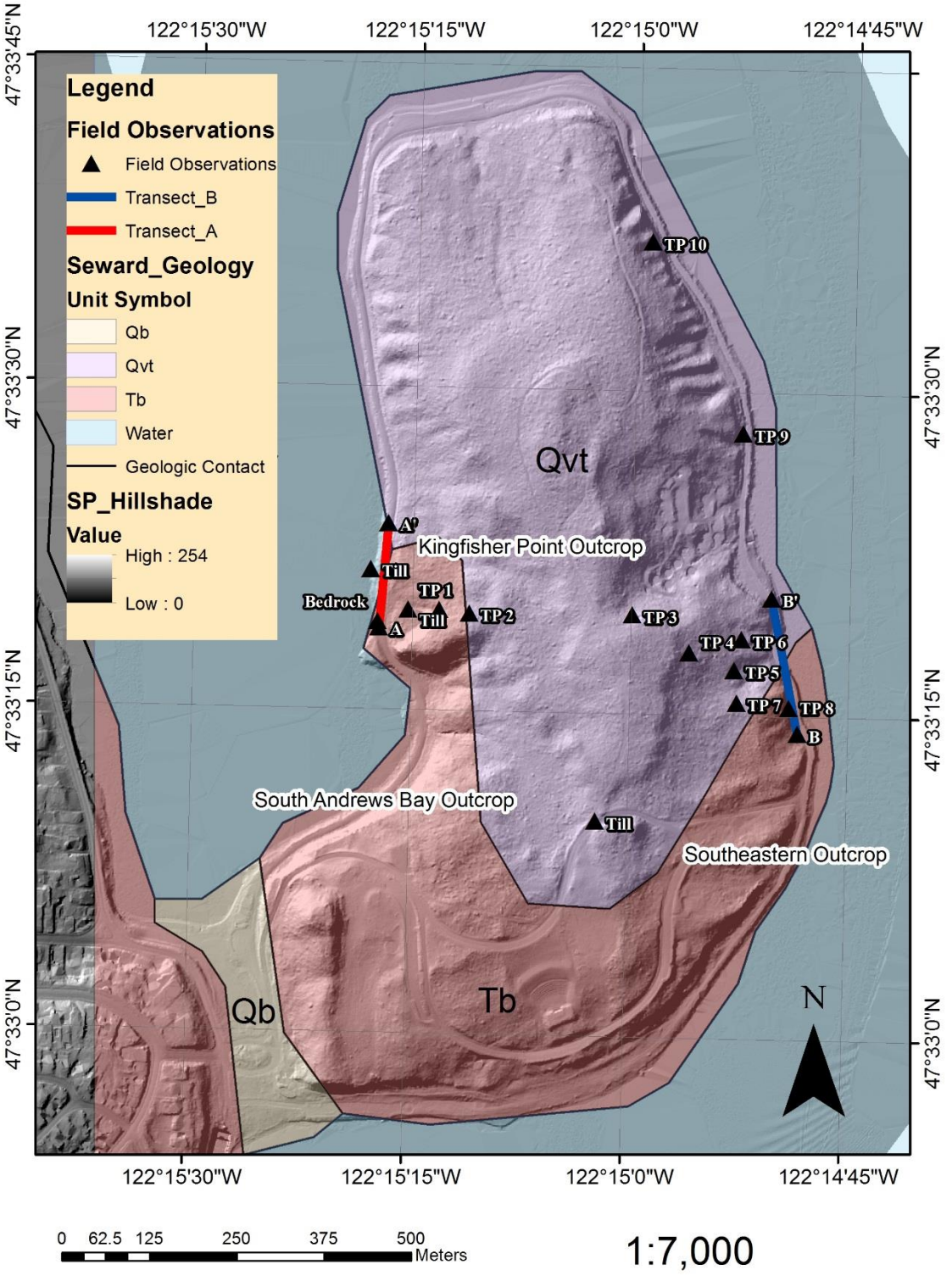

Figure 10: Ten small test pits were dug by hand to better understand the distribution of till and bedrock throughout the park. These investigations along with the mapped geology were used to determine the marked transect locations for geophysical work.

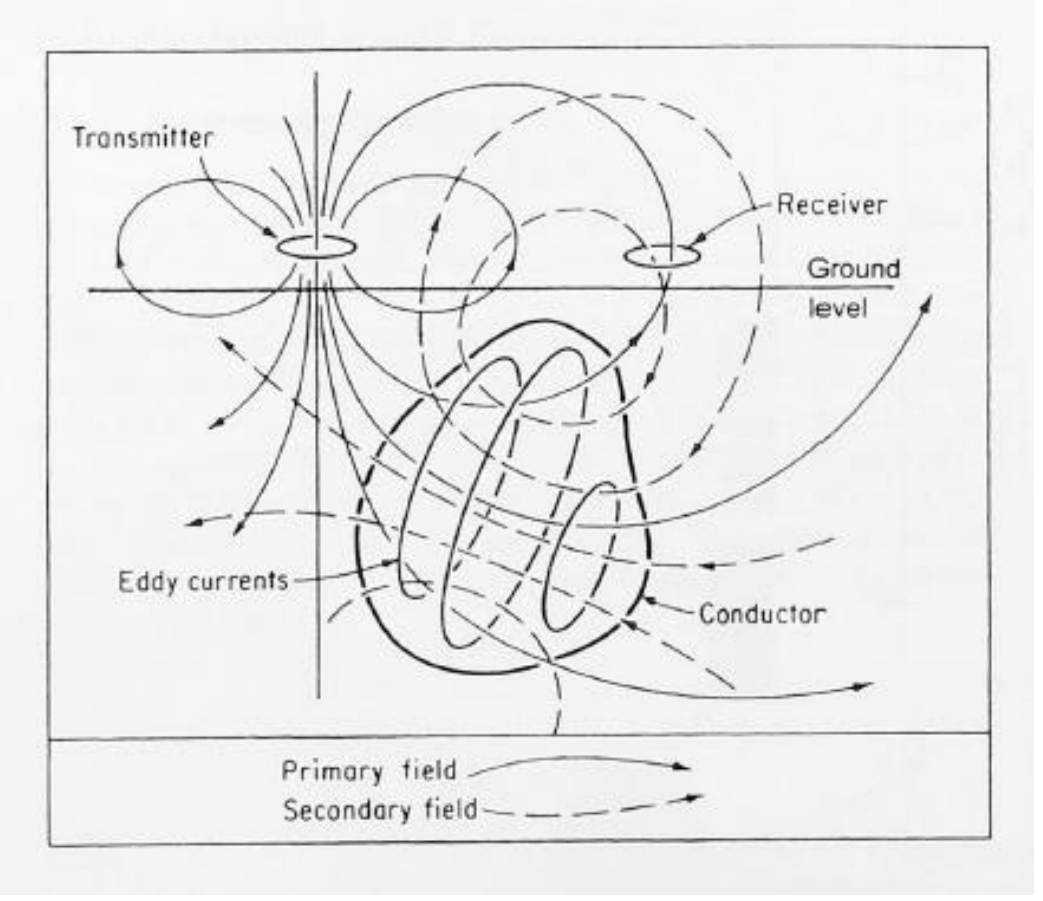

Figure 11: Convolution of the primary field produced by the GPR antenna and the secondary field generated when the EM wave travels through the ground. The Receiver records the combination of both fields. GPR processing is used to deconvolute the signal and determine the geometry and size of conductive materials (Reynolds, 1997).

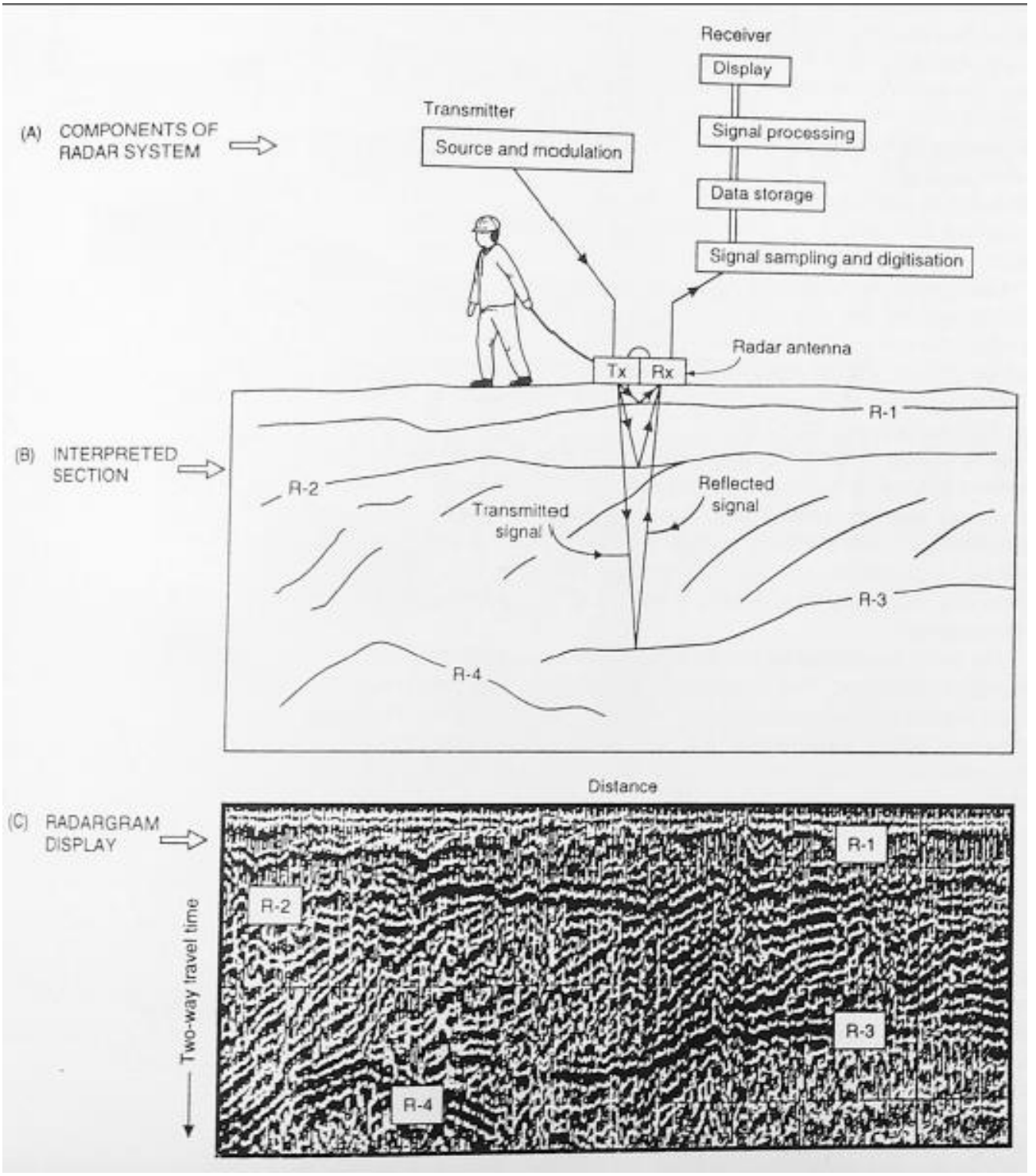

Figure 12: Schematic of a typical GPR survey taken from Reynolds (1997). The final deliverable of a GPR survey is the associated radargram.

Figure 13: Author shown with the MALA GX 80 MHz GPR instrument. This was the ground-penetrating radar system used in the geophysical investigation.

Material	ε_r	V(mm/ns)
Air	1	300
Water (fresh)	81	33
Water (sea)	81	33
Polar snow	1.4–3	194–252
Polar ice	3–3.15	168
Temperate ice	3.2	167
Pure ice	3.2	167
Freshwater lake ice	4	150
Sea ice	2.5–8	78–157
Permafrost	1–8	106–300
Coastal sand (dry)	10	95
Sand (dry)	3–6	120–170
Sand (wet)	25–30	55–60
Silt (wet)	10	95
Clay (wet)	8–15	86–110
Clay soil (dry)	3	173
Marsh	12	86
Agricultural land	15	77
Pastoral land	13	83
Average 'soil'	16	75
Granite	5–8	106–120
Limestone	7–9	100–113
Dolomite	6.8–8	106–115
Basalt (wet)	8	106
Shale (wet)	7	113
Sandstone (wet)	6	112
Coal	4–5	134–150
Quartz	4.3	145
Concrete	6–30	55–112
Asphalt	3–5	134–173
PVC, Epoxy, Polyesters	3	173

Figure 14: Typical values of dielectric constant (ε_r) and the associated EM velocity for Earth materials (Reynolds, 1997).

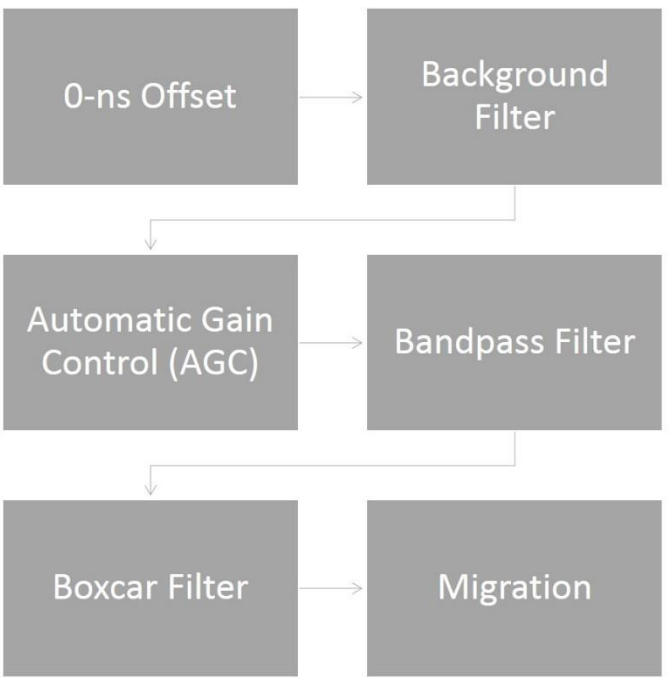

Figure 15: Summary of the GPR Processing Steps

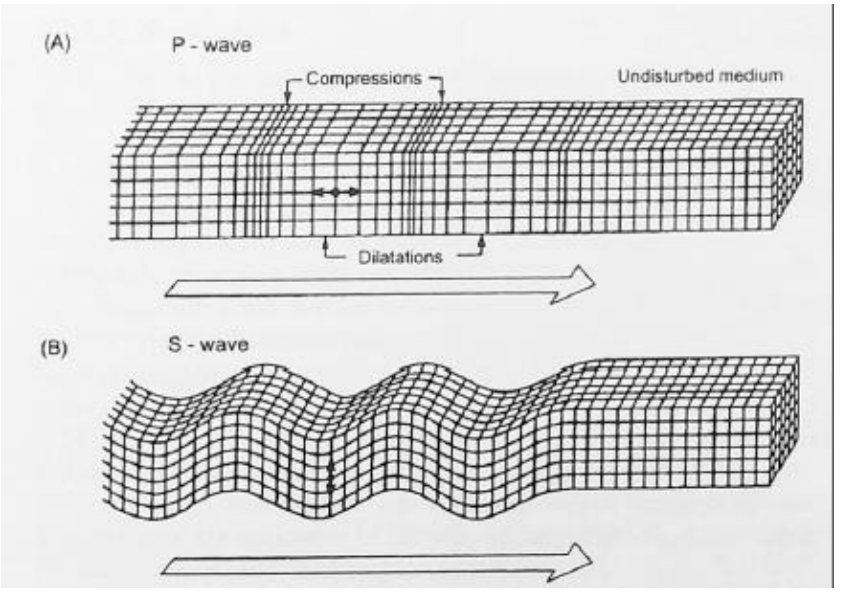

Figure 16: Differences in propagation of compressional (p)-wave and shear (s)-wave (Reynolds, 1997).

Type of formation	P wave velocity (m/s)	S wave velocity (m/s)
Scree, vegetal soil	300-700	100-300
Dry sands	400-1200	100-500
Wet sands	1500-2000	400-600
Saturated shales and clays	1100-2500	200-800
Marls	2000-3000	750-1500
Saturated shale and sand sections	1500-2200	500-750
Porous and saturated sandstones	2000-3500	800-1800
Limestones	3500-6000	2000-3300
Chalk	2300-2600	1100-1300
Salt	4500-5500	2500-3100
Anhydrite	4000-5500	2200-3100
Dolomite	3500-6500	1900-3600
Granite	4500-6000	2500-3300
Basalt	5000-6000	2800-3400
Gneiss	4400-5200	2700-3200
Coal	2200-2700	1000-1400
Water	1450-1500	-
Ice	3400-3800	1700-1900
Oil	1200-1250	-

Figure 17: Body wave velocities in Earth materials. (Reynolds,1997).

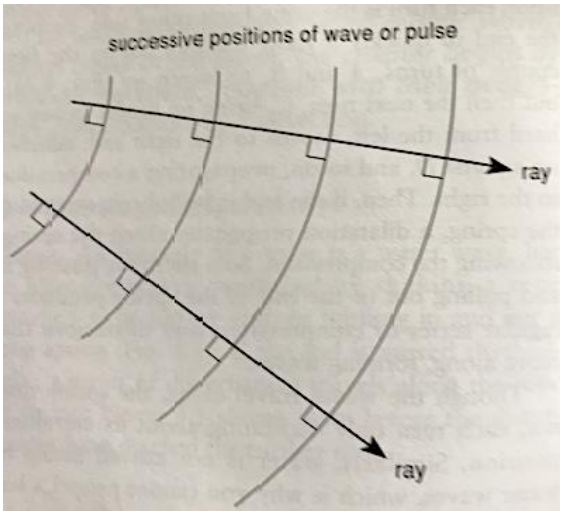

Figure 18: The path of a portion of the wave front, or pulse, forms a ray. Rays are always orthoganol to wave fronts (Mussett & Khan, 2000).

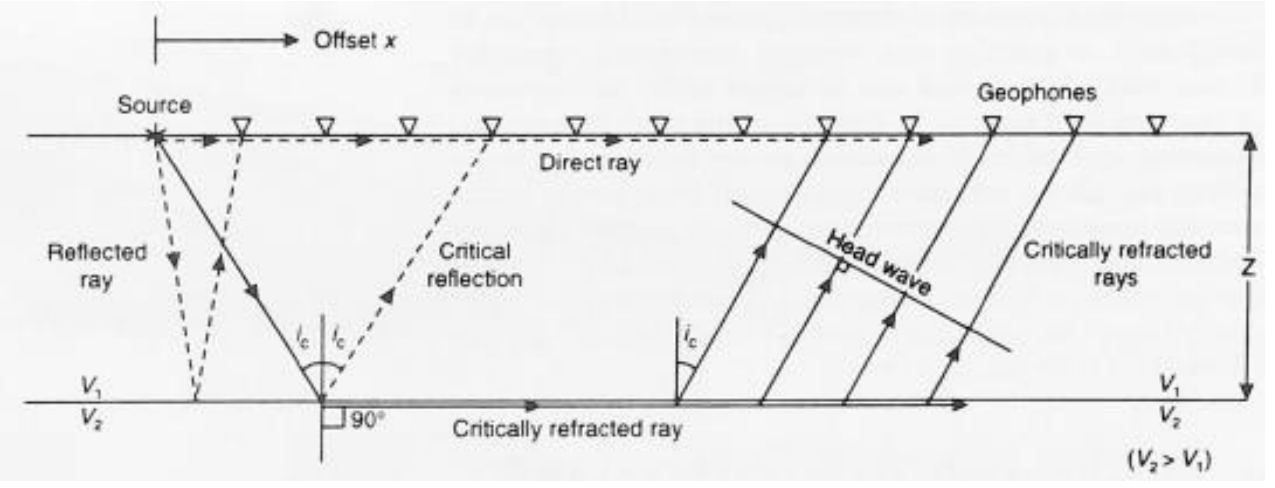

Figure 19: Schematic of a simple two-layer refraction survey (Reynolds, 1997)

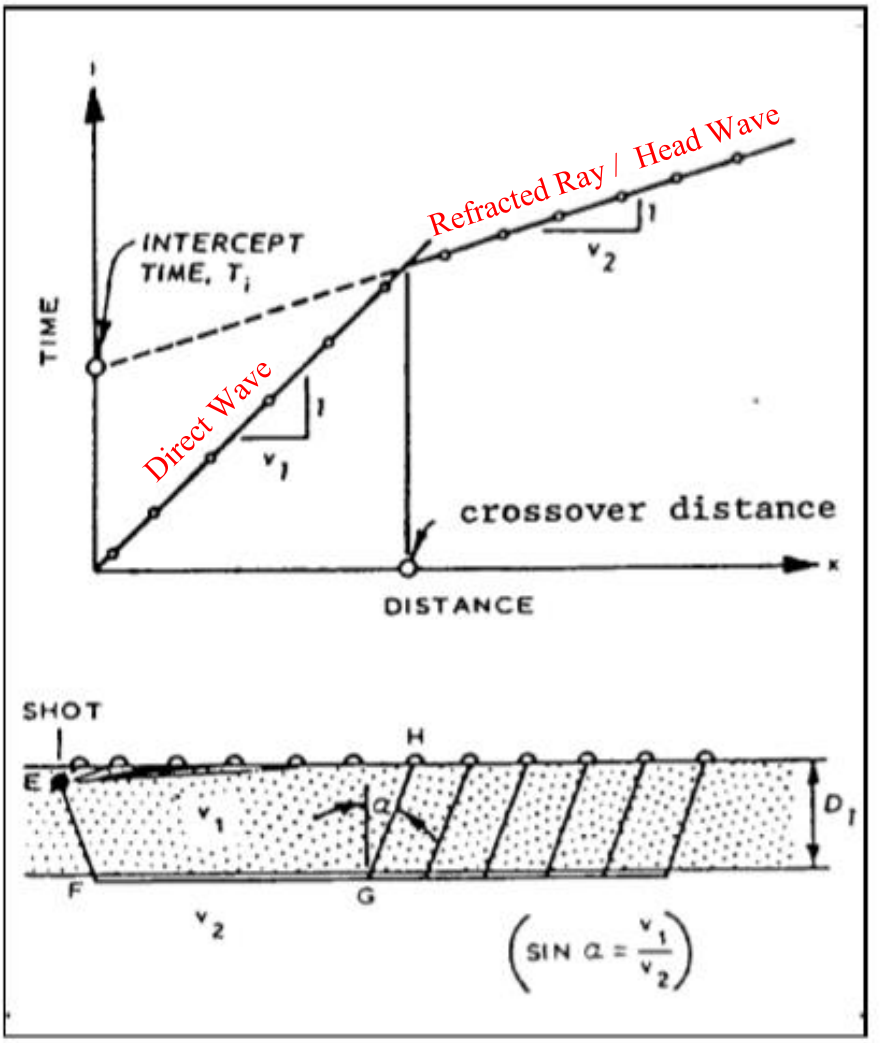

Figure 20: Simple two-layer case with plane, parallel boundaries. At short distances, the direct wave arrives first. However, after the critical distance, the refracted wave begins to arrive first (Griffin, 1995).

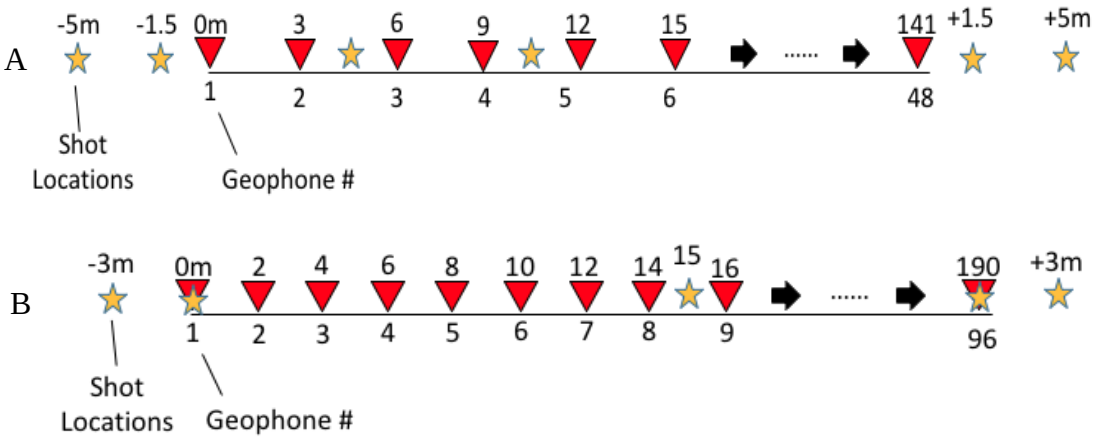

Figure 21: Seismic surveys were conducted under ideal sunny conditions with dry ground conditions. A) Transect A array geometry. The array was 141 meters in length with a 3 m spacing interval. B) Transect B array geometry. The array was 190 meters in length with a 2 m spacing interval.

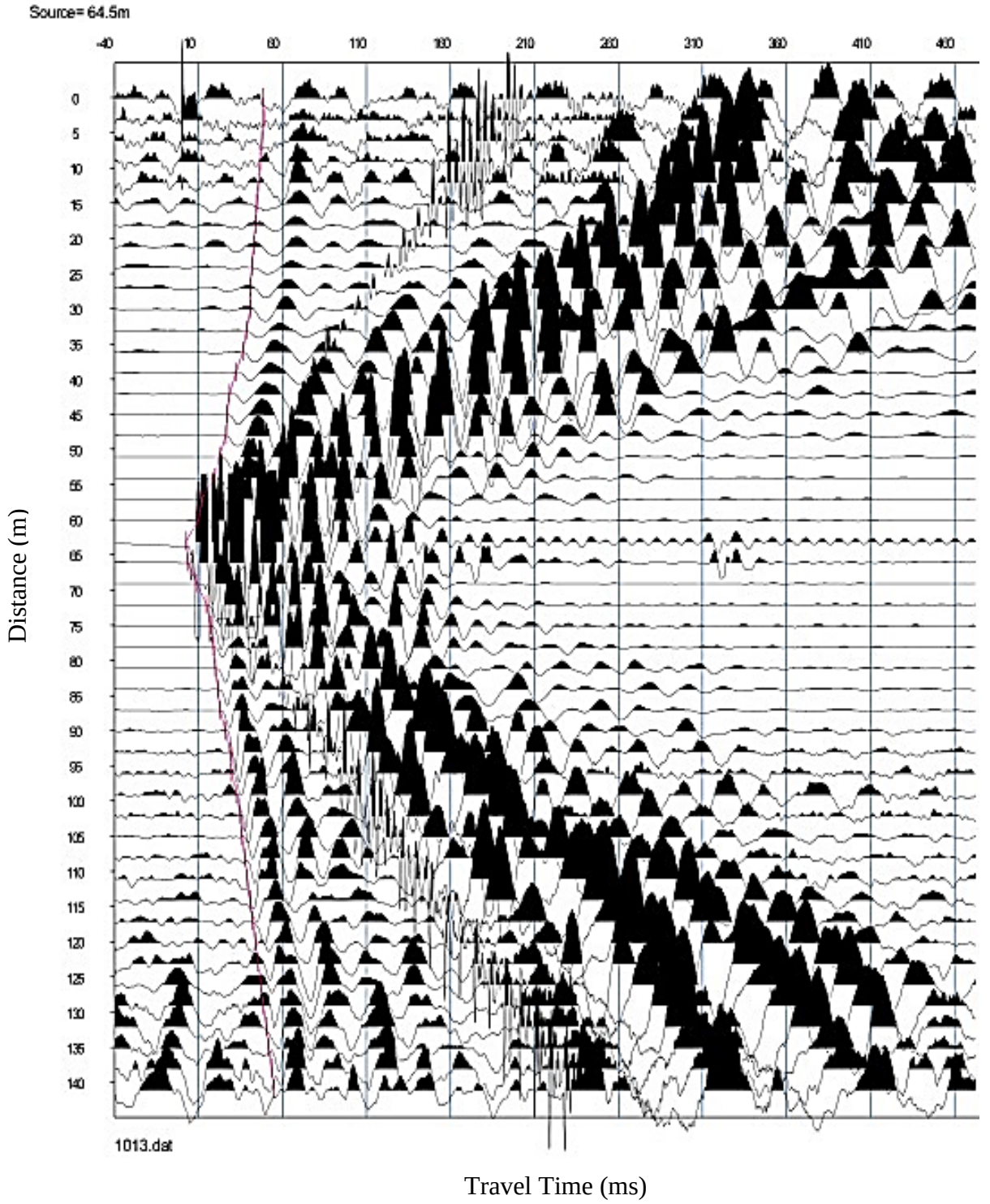

Figure 22: Selection of p-wave first arrivals in SeisImager/2D for a single shot gather at Transect A. The selection of first arrivals can be observed as the pink line. From this image we can observe that p-waves arrive first making them possible to identify in each geophone signal.

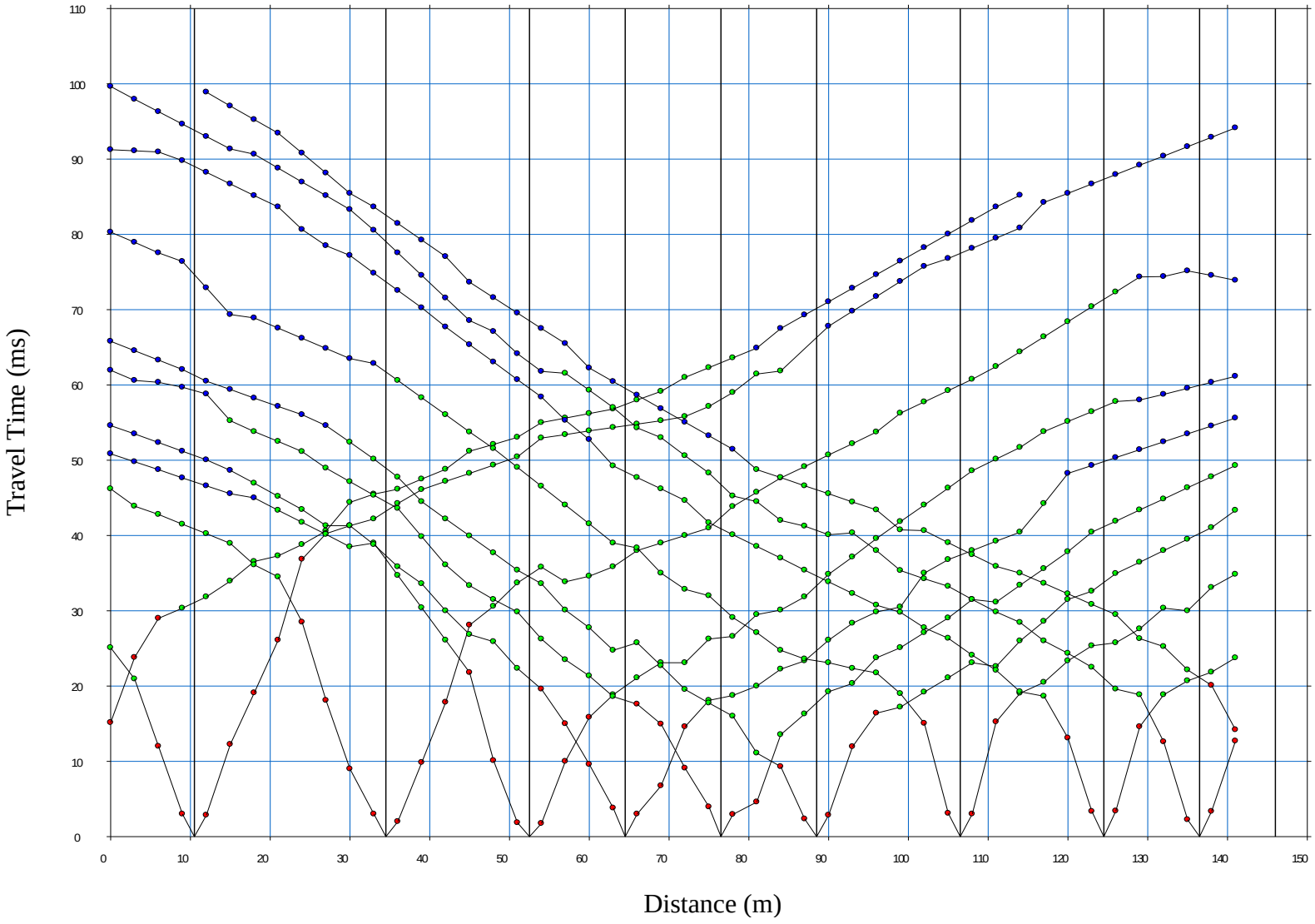

Figure 23: Transect A p-wave first arrivals for all shot gathers. Two to three potential layers were identified by observing breaks in slope in the travel time versus distance plot. The breaks in slope indicate a change in Vp. These layers are color coded in red, green, and blue respectively.

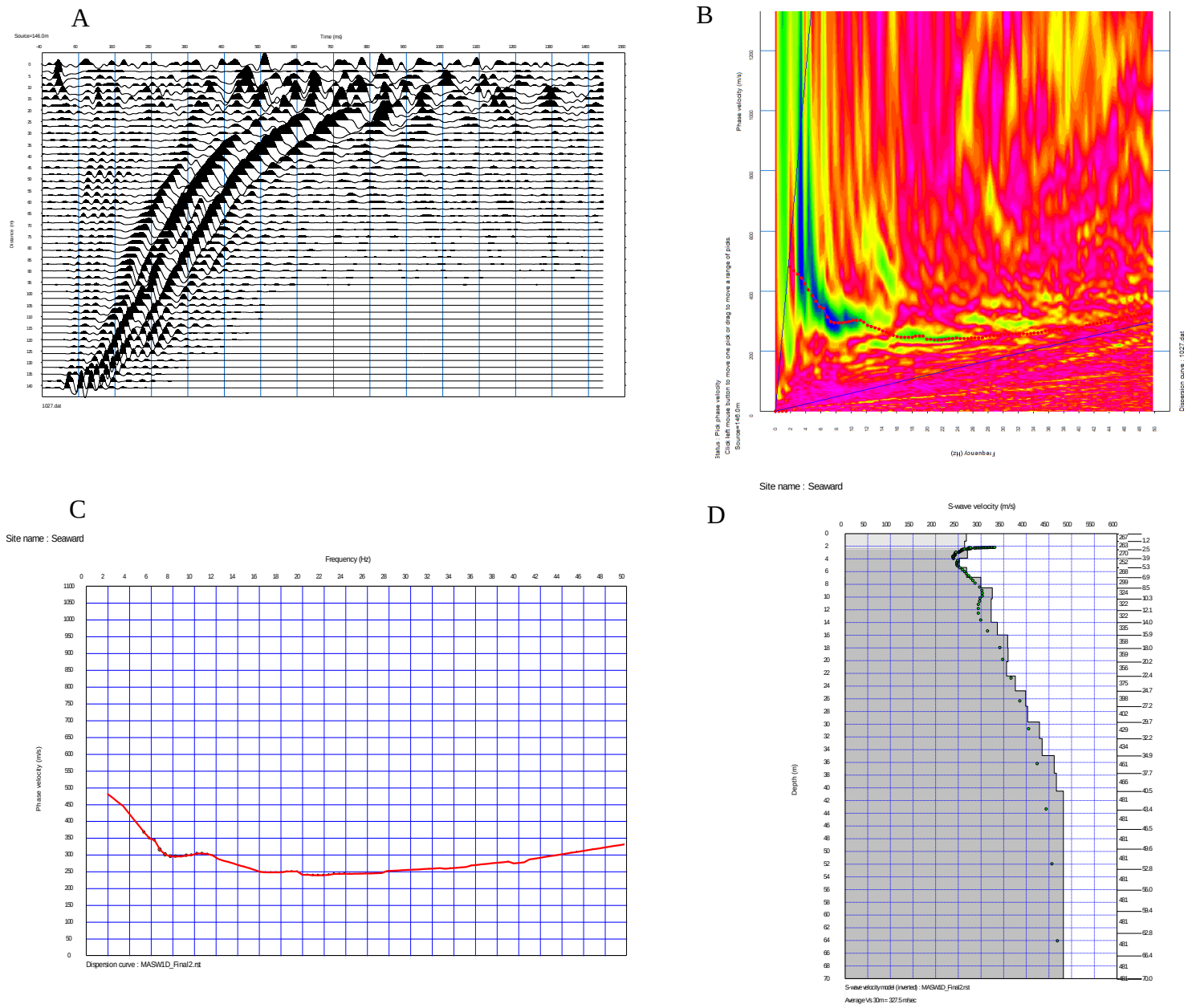

Figure 24: 1-D MASW analysis process using transect A data. A) Raw data from a single shot gather recorded from the geophones. B) Dispersion image created by software. High amplitude frequencies are represented in blue and green. C) Dispersion curve selected from the fundamental mode found on the dispersion image. D) Final 1-D V_s profile constructed through tomographic iteration.

A

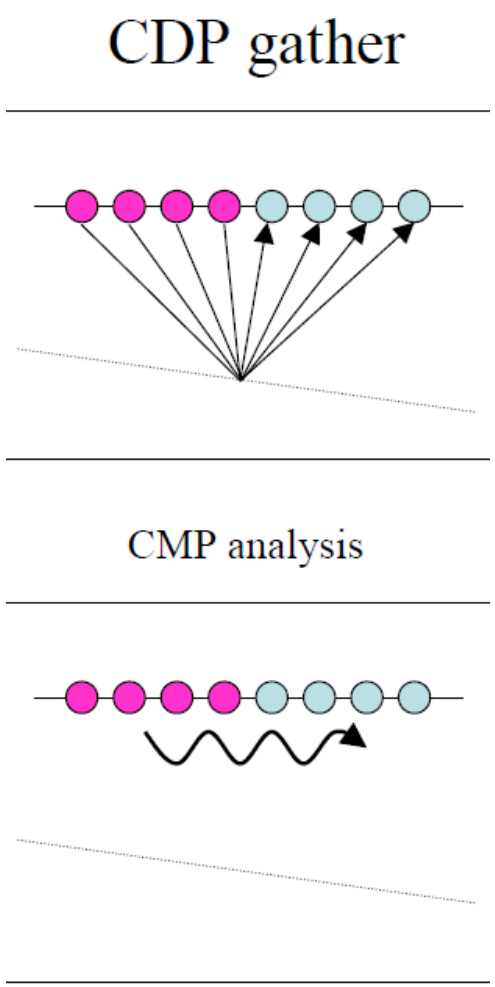

B

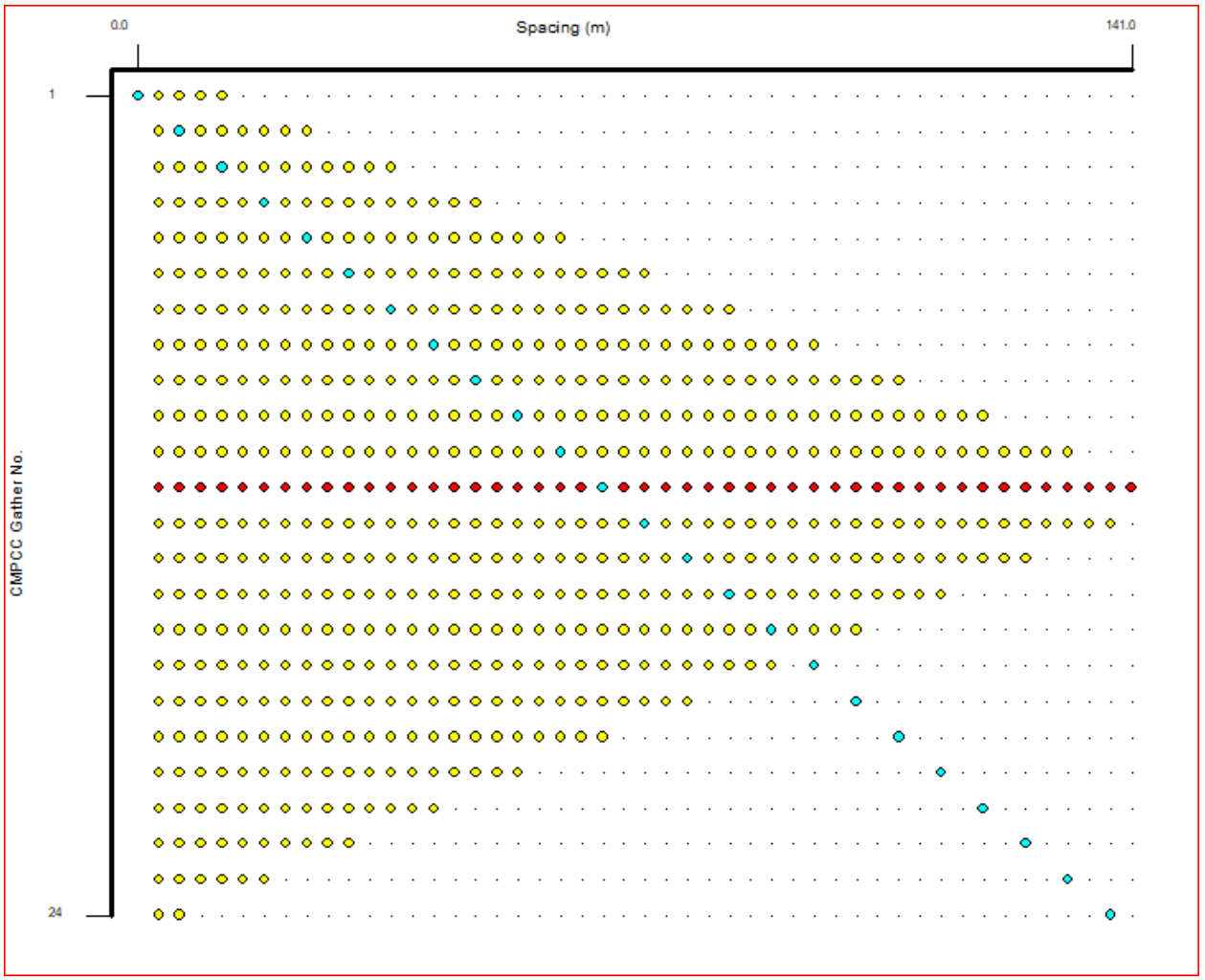

Figure 25: A) Comparison of common depth point (CDP) method used in seismic reflection surveying versus common midpoint (CMP) used for surface waves (Geometrics Inc., 2009). B) Common midpoint cross-correlation (CMPCC) results for transect A. Shot locations within the array are represented by the teal points. The number of yellow dots represent the frequency that a shot point location was visited. The shot location near the center of the array (in red) was visited most frequently. Therefore, data is most reliable in the center of the array and confidence decreases laterally.

Grade	Description	Field identification	Approx. range of uniaxial compressive strength (MPa)
S1	Very soft clay	Easily penetrated several inches by fist	<0.025
S2	Soft clay	Easily penetrated several inches by thumb	0.025–0.05
S3	Firm clay	Can be penetrated several inches by thumb with moderate effort	0.05–0.10
S4	Stiff clay	Readily indented by thumb but penetrated only with great effort	0.10–0.25
S5	Very stiff clay	Readily indented by thumbnail	0.25–0.50
S6	Hard clay	Indented with difficulty by thumbnail	>0.50
R0	Extremely weak rock	Indented by thumbnail	0.25–1.0
R1	Very weak rock	Crumbles under firm blows with point of geological hammer, can be peeled by a pocket knife	1.0–5.0
R2	Weak rock	Can be peeled by a pocket knife with difficulty, shallow indentations made by firm blow with point of geological hammer	5.0–25
R3	Medium strong rock	Cannot be scraped or peeled with a pocket knife, specimen can be fractured with single firm blow of geological hammer	25–50
R4	Strong rock	Specimen requires more than one blow of geological hammer to fracture it	50–100
R5	Very strong rock	Specimen requires many blows of geological hammer to fracture it	100–250
R6	Extremely strong rock	Specimen can only be chipped with geological hammer	>250

Term	Description	Grade
Fresh	No visible sign of rock material weathering; perhaps slight discolouration on major discontinuity surfaces.	I
Slightly weathered	Discolouration indicates weathering of rock material and discontinuity surfaces. All the rock material may be discoloured by weathering and may be somewhat weaker externally than in its fresh condition.	II
Moderately weathered	Less than half of the rock material is decomposed and/or disintegrated to a soil. Fresh or discoloured rock is present either as a continuous framework or as corestones.	III
Highly weathered	More than half of the rock material is decomposed and/or disintegrated to a soil. Fresh or discoloured rock is present either as a discontinuous framework or as corestones.	IV
Completely weathered	All rock material is decomposed and/or disintegrated to soil. The original mass structure is still largely intact.	V
Residual soil	All rock material is converted to soil. The mass structure and material fabric are destoyed. There is a large change in volume, but the soil has not been significantly transported.	VI

Figure 26: ISRM 1978 field guides for the classification of uniaxial compressive strength and weathering.

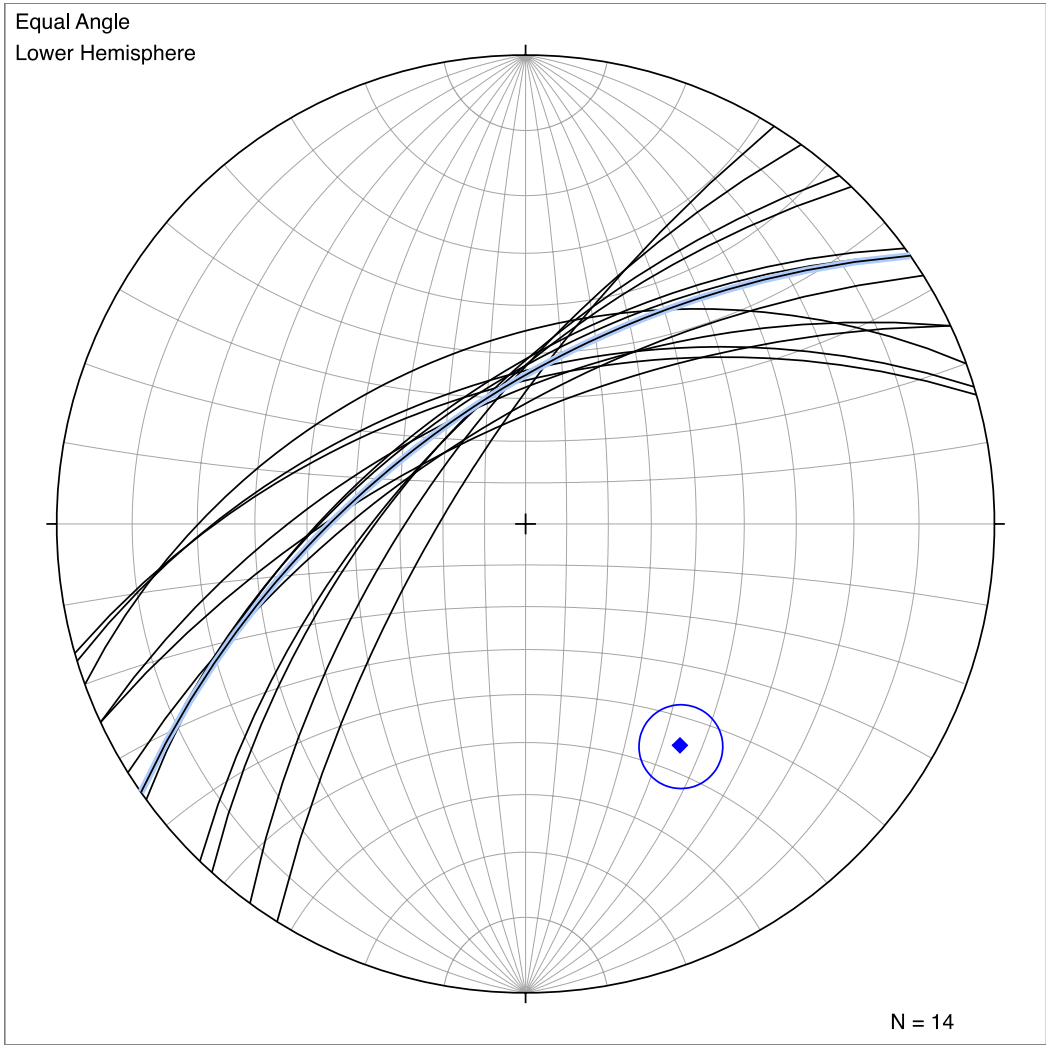

Figure 27: Blakeley Formation bedding plane measurement results. Thirteen measurements were taken in total. The mean pole vector can be observed as the blue dot. The mean great circle (S55W, 60N) is highlighted in blue.

Figure 28: A) Example of a test pit where saprolitic bedrock was found at the base of the pit in the form of core stones. B) Example of a test pit where till and/or colluvium was found throughout the entire depth of the pit. C) Example of a test pit where a thin veneer of soil/colluvium covered bedrock.

S

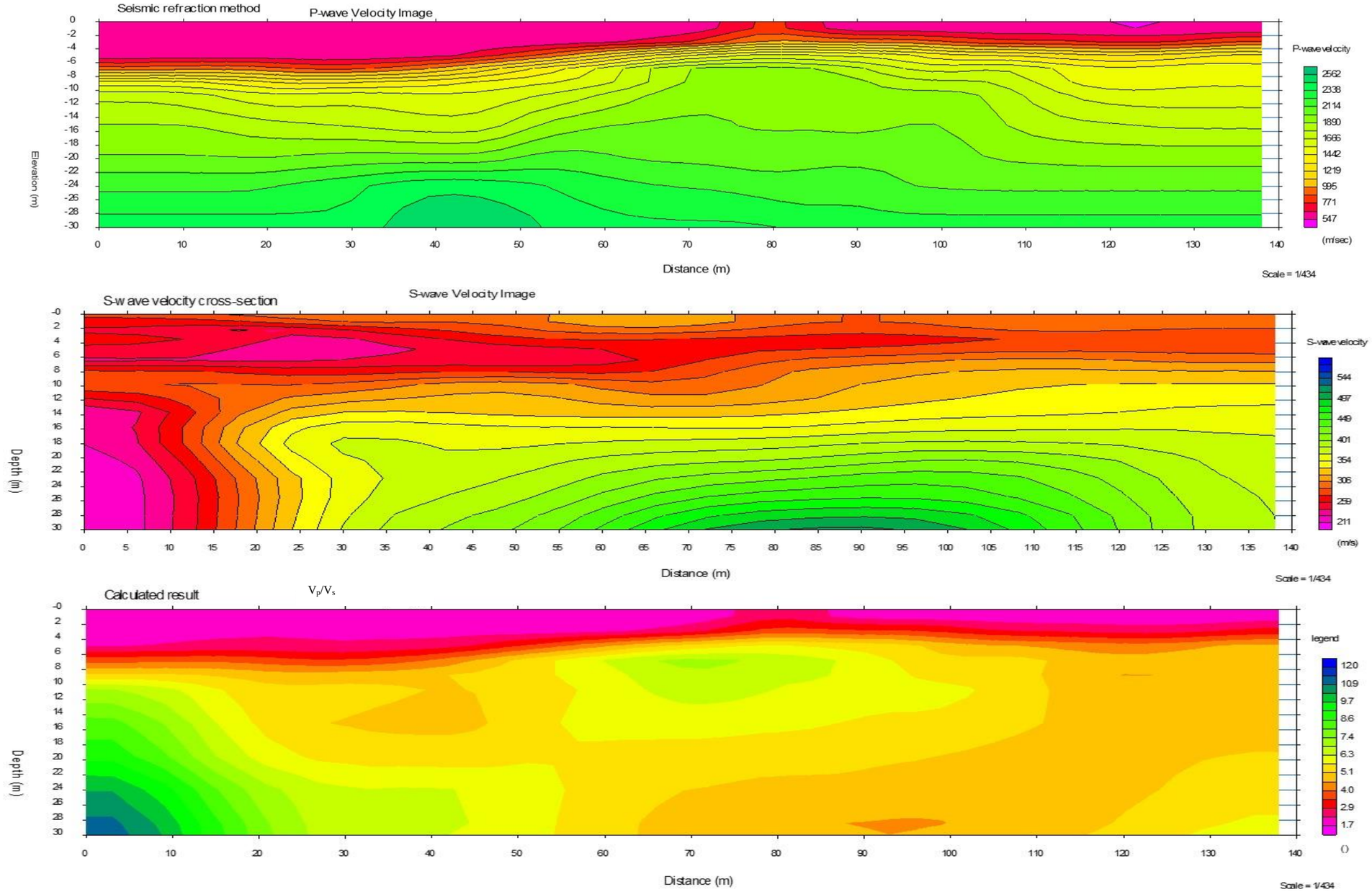

N

A

A’

Figure 29: Transect A two-dimensional seismic models generated in Geometrics software. This data was collected on the western side of Seward Park. Top: V_p model. Middle: V_s model. Bottom: V_p/V_s model. VE 1:1.

S

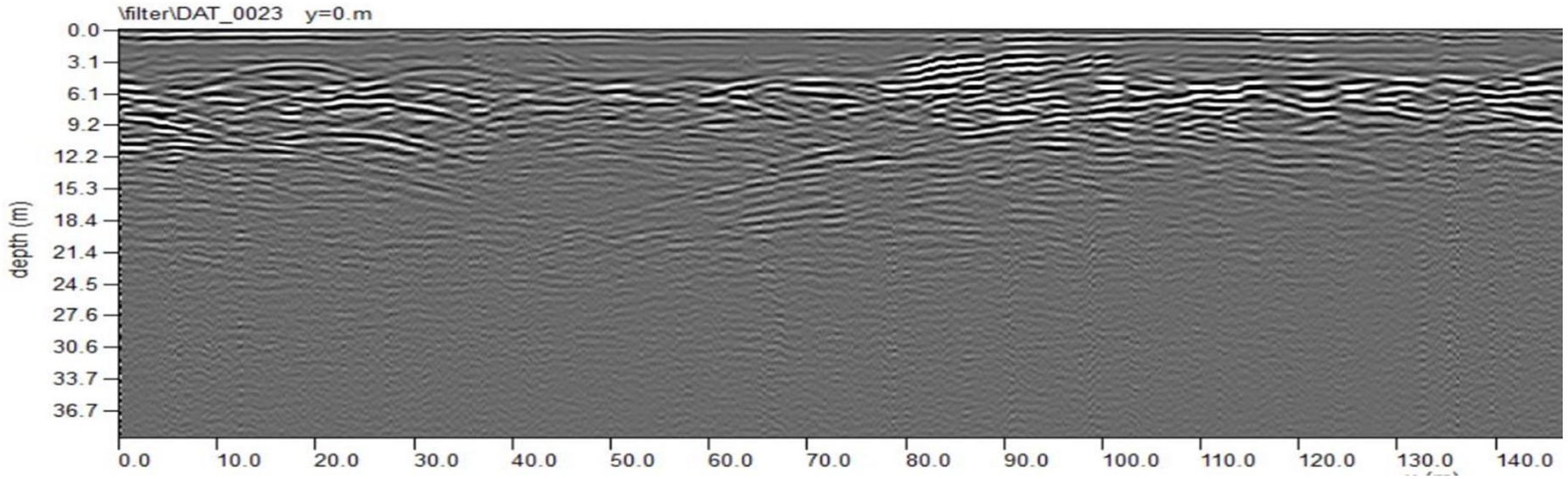

N

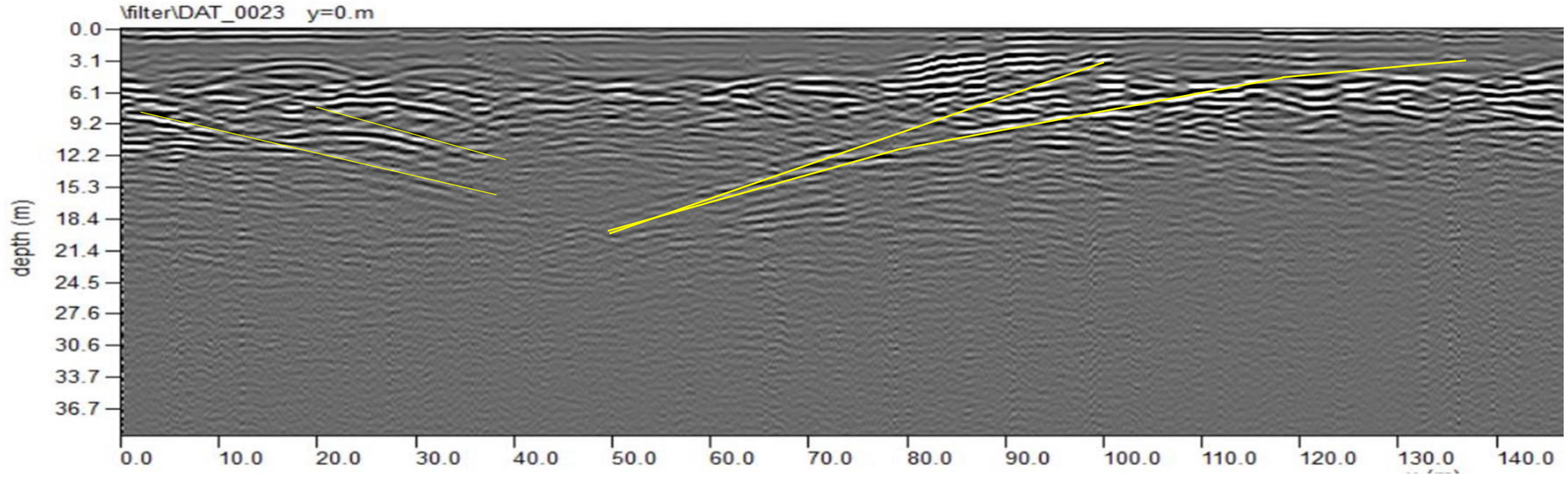

A

A’

Figure 30: Transect A processed GPR data. This data was collected on the western side of Seward Park. Persistent reflectors have been marked in the second copy of the image. The yellow lines represent persistent reflective barriers.

S

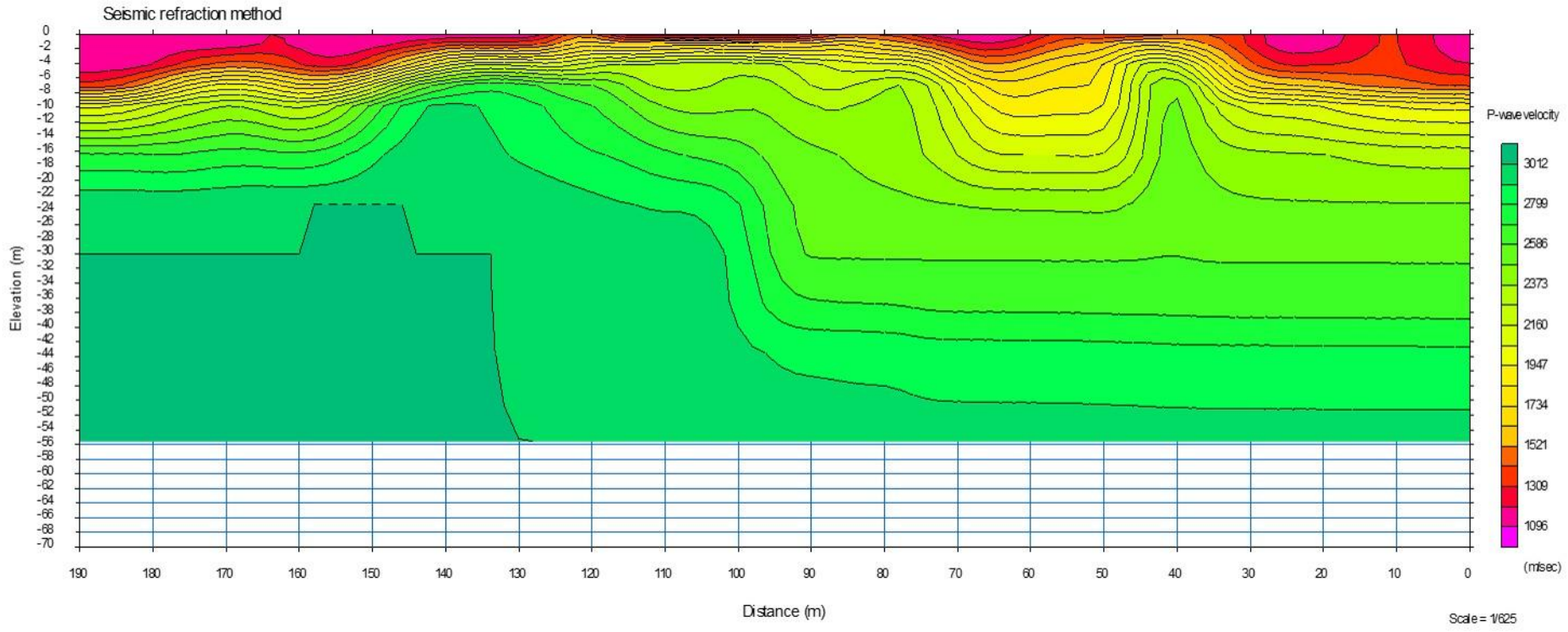

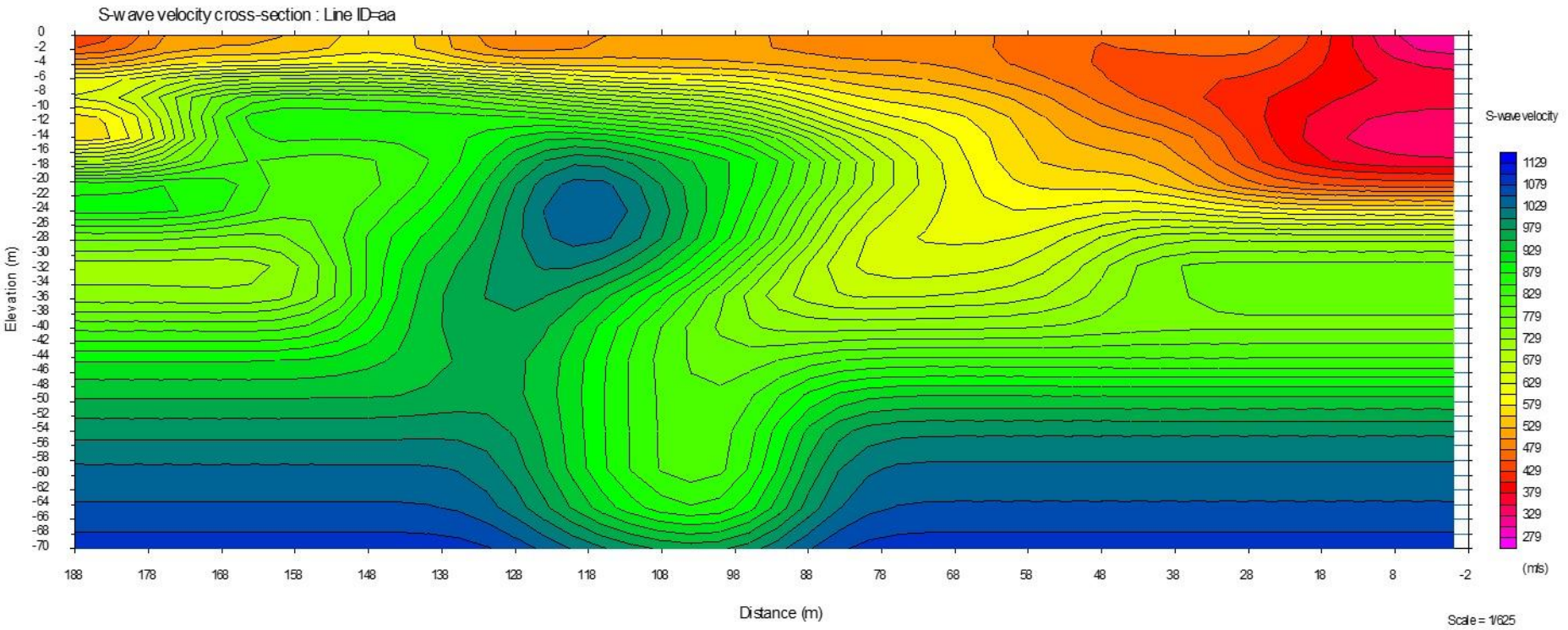

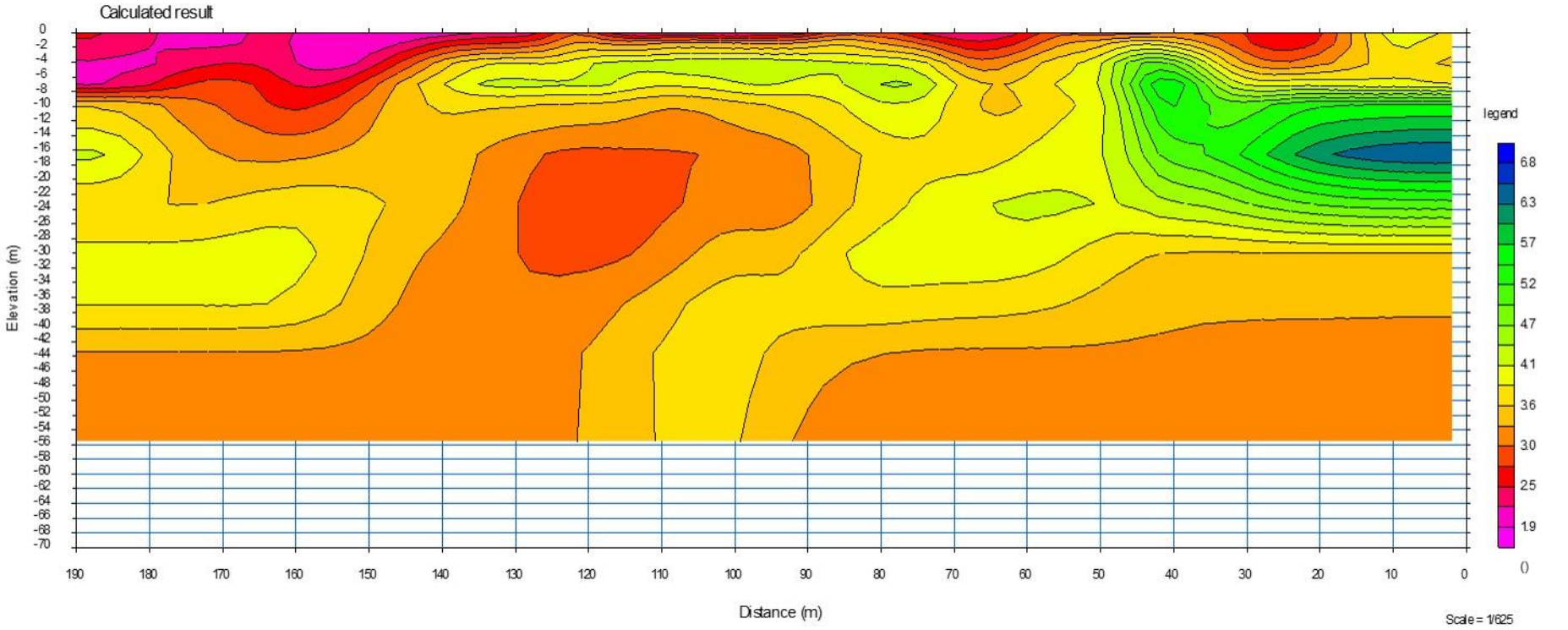

B

B’

Figure 31: Transect B two-dimensional seismic models generated in the Geometrics software. This data was collected on the eastern side of Seward Park. Top: V_p model. Middle: V_s model. V_p/V_s model. VE 1:1.

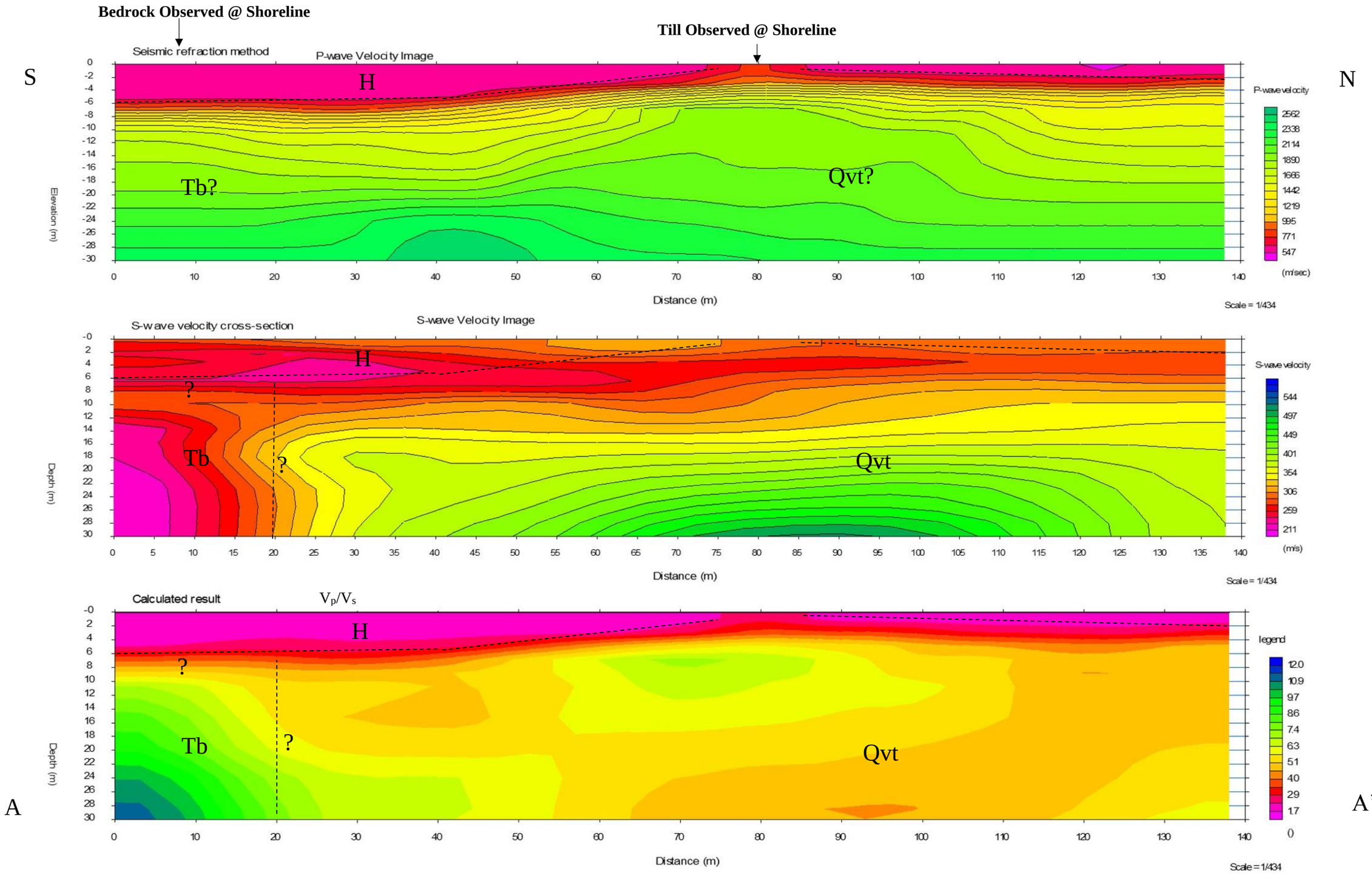

Figure 32: Transect A interpreted geologic units overlaid on the seismic models. Dashed lines represent potential locations of material transition. Qvt = Vashon Till, H = Holocene deposits (unconsolidated), Tb = Blakely Formation. VE 1:1.

S

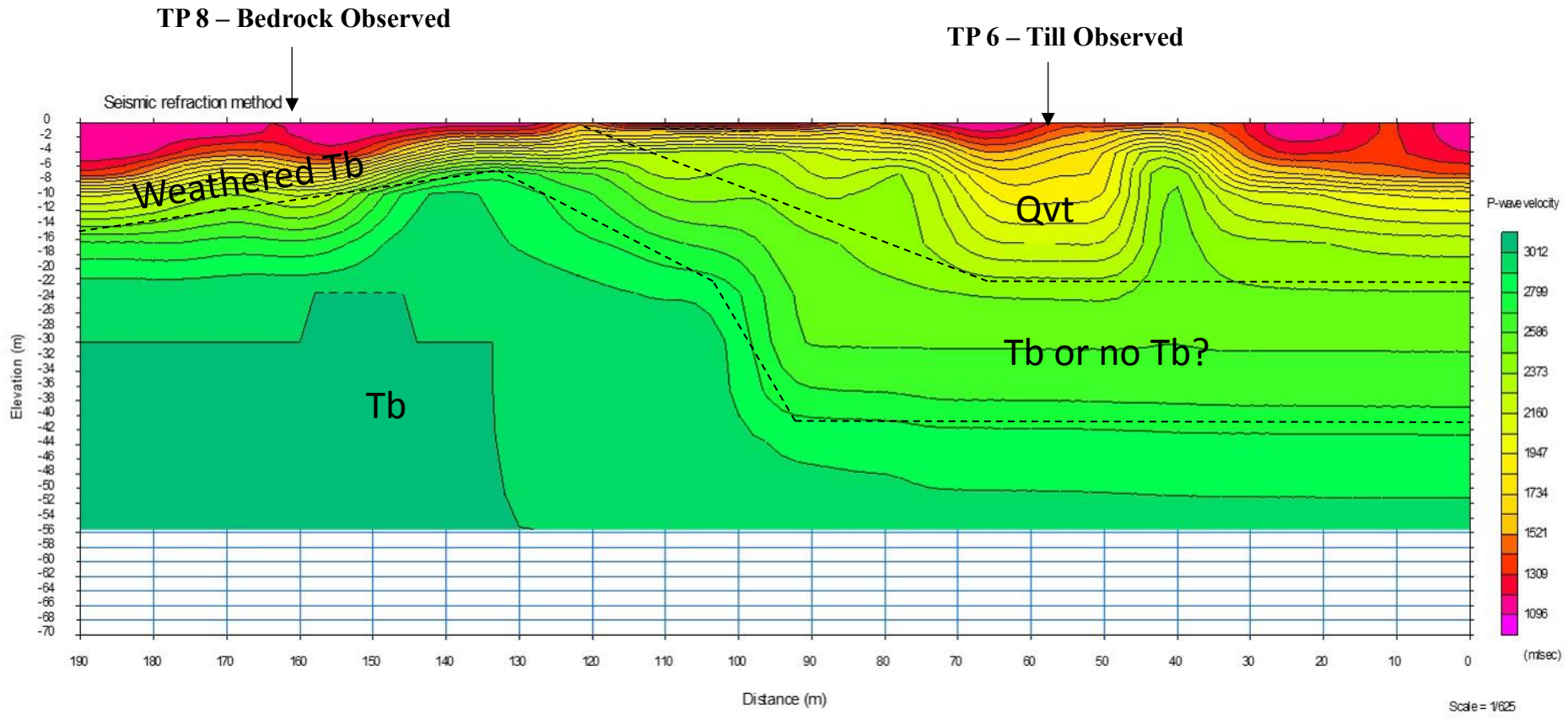

N

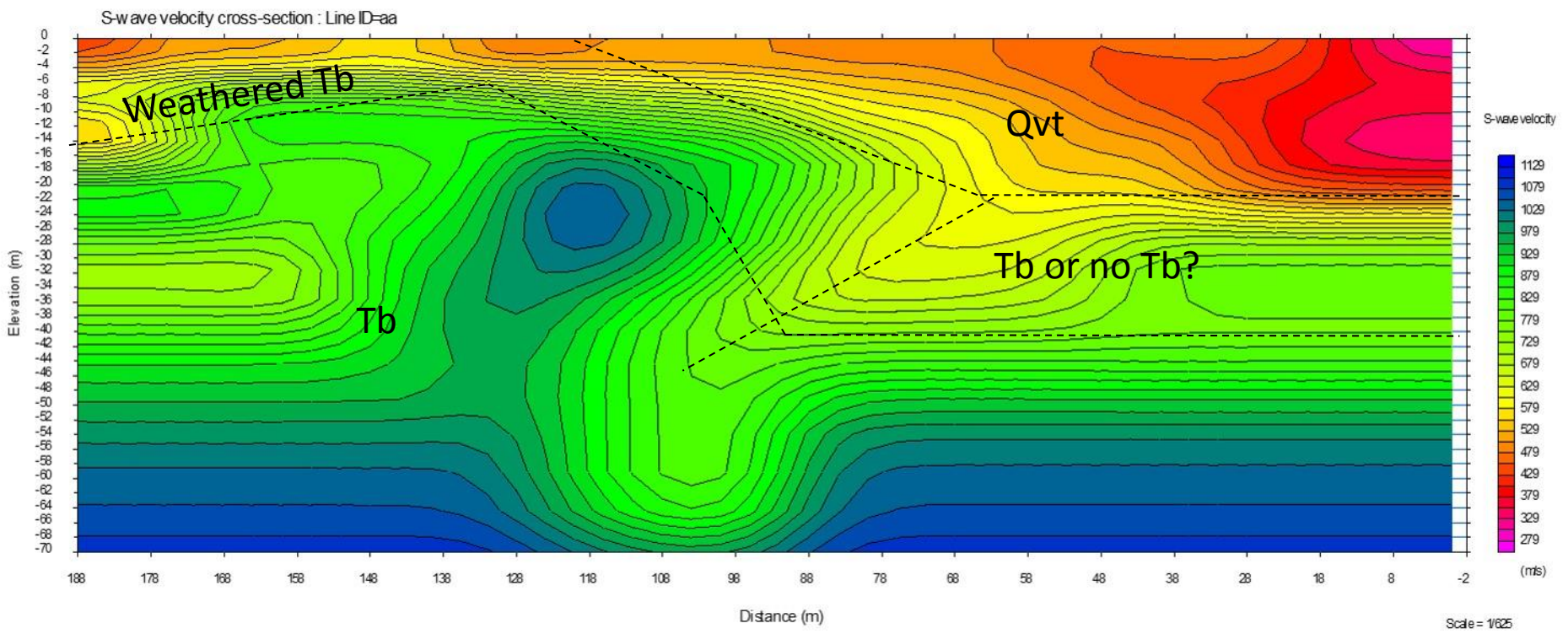

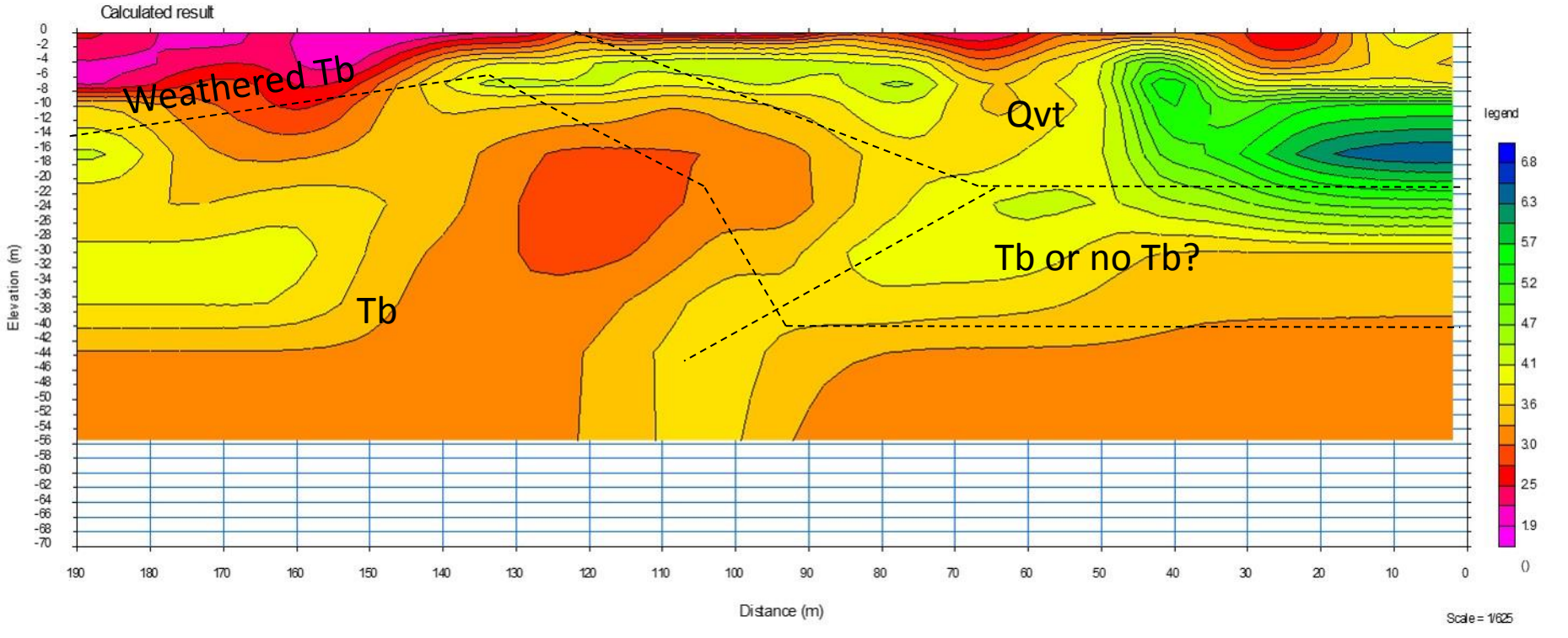

B

B’

Figure 33: Transect B interpreted geologic units overlaid on the seismic models. Dashed lines represent potential areas of material transition. Qvt = Vashon till, H = Holocene deposits (unconsolidated), Tb = Blakeley Formation. VE 1:1.

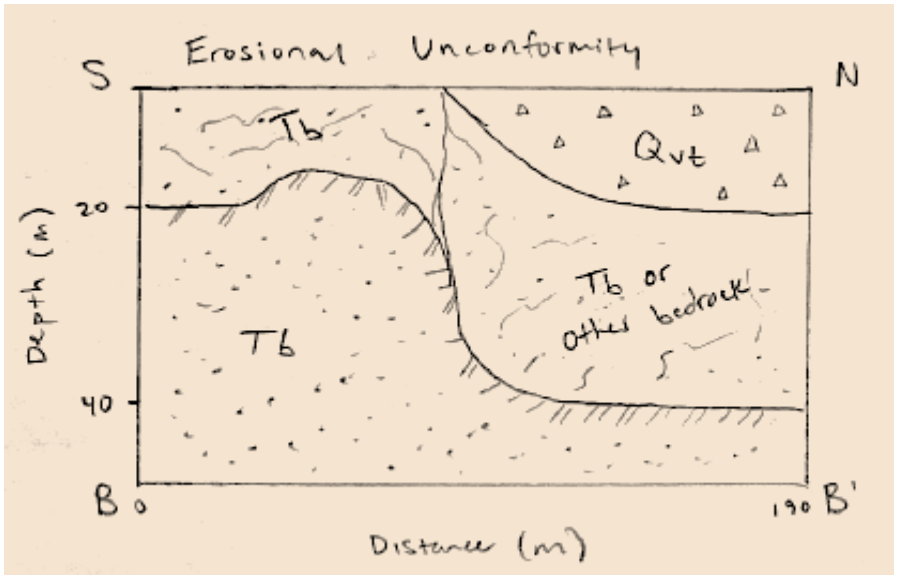

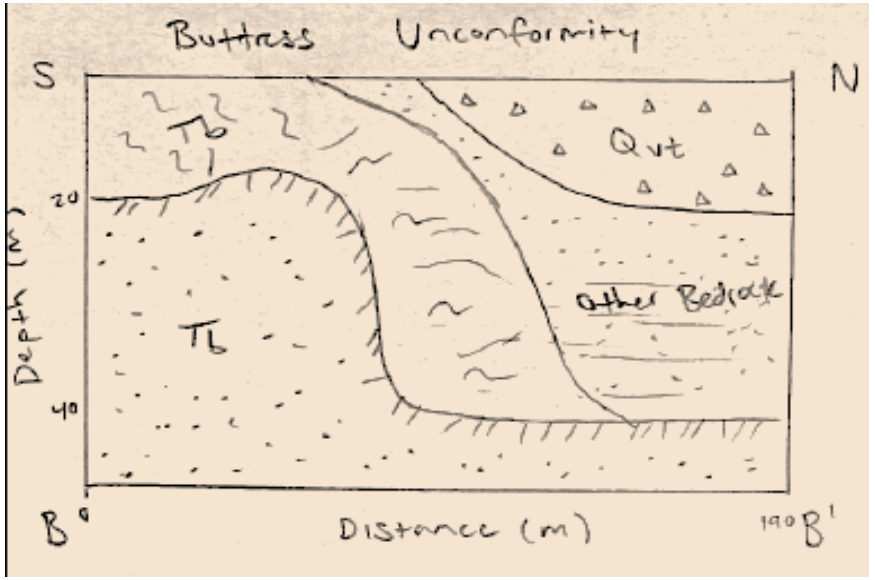

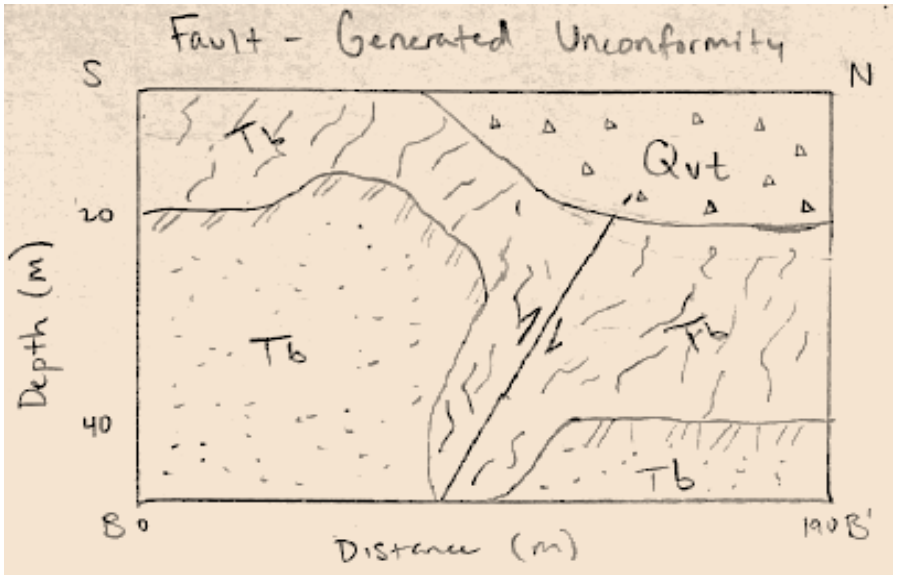

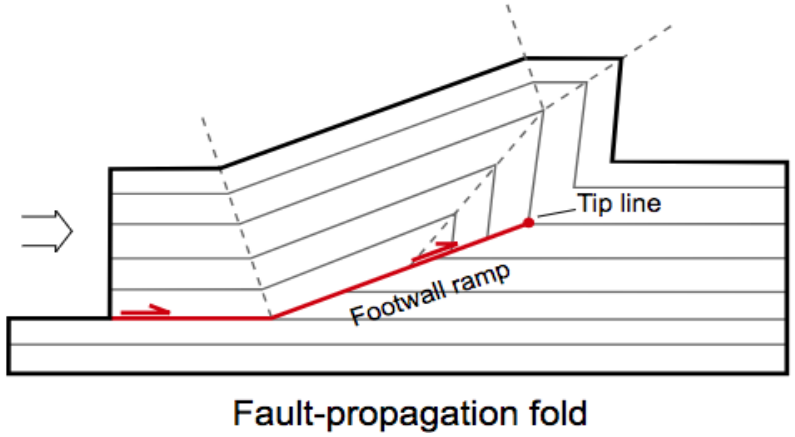

Figure 34: Three possible mechanisms for the subsurface geometry observed along the Seward Park unconformity.

Appendices

Appendix A: GPR Processing

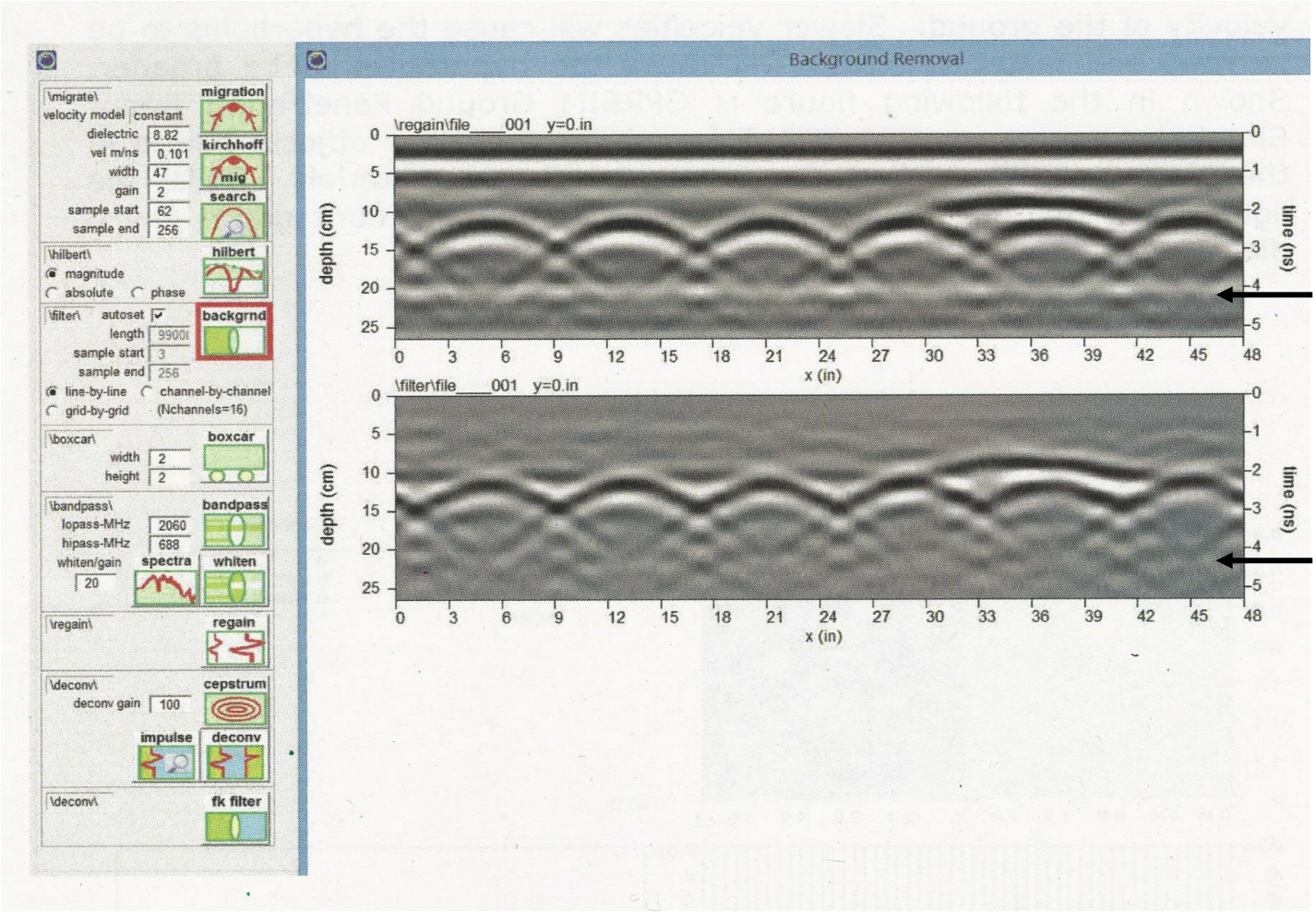

Figure A-1: Example of a background filter (Goodman, 20009). We can see how banding noises are removed from the radargram. Banding noises are identifiable because they are consistent throughout the entire survey length.

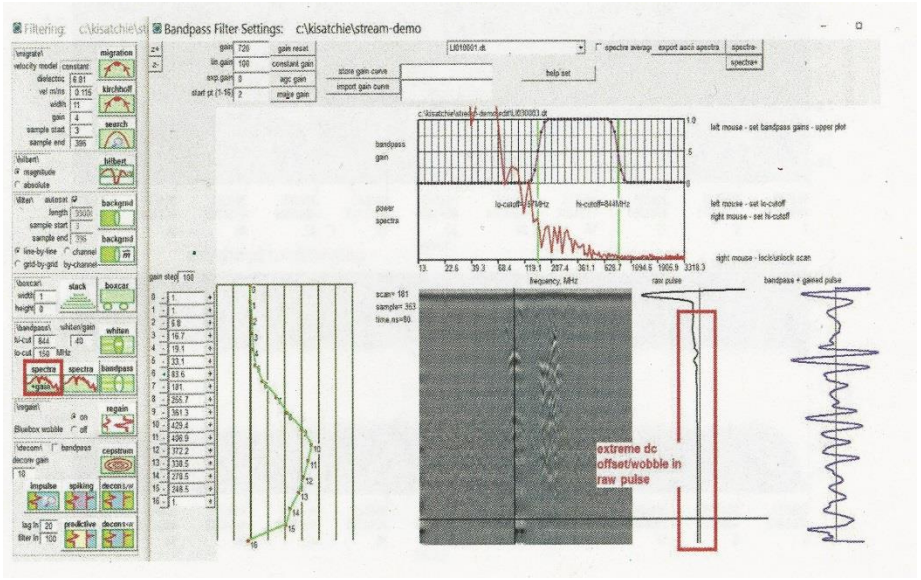

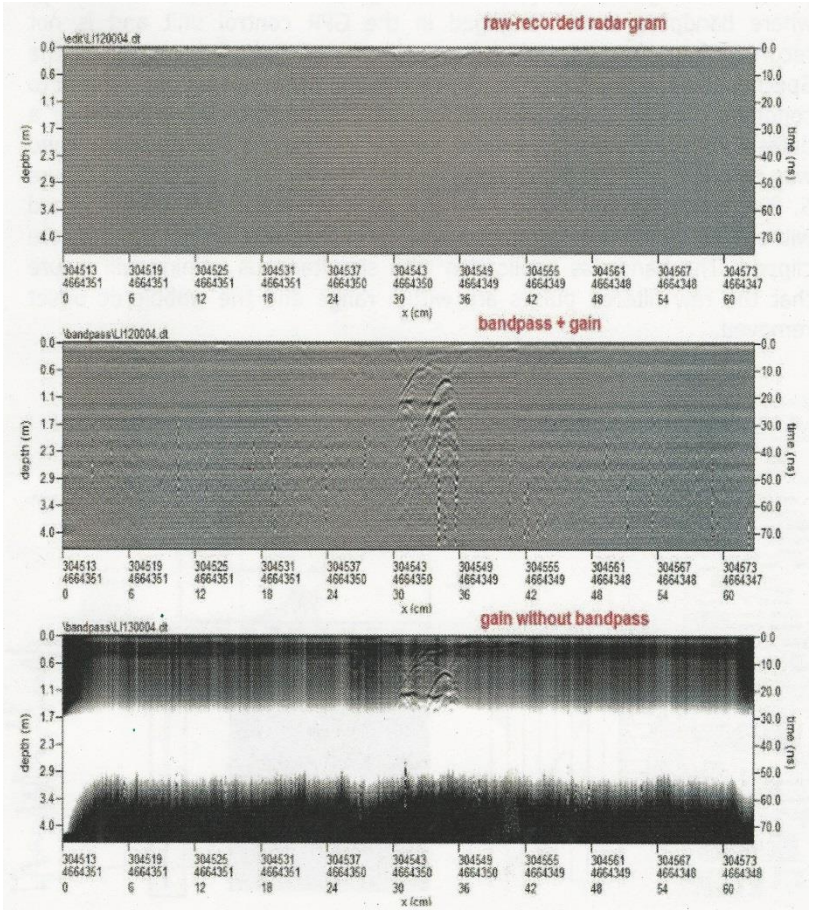

Figure A-2: Example of AGC and bandpass filters being applied to raw data (Goodman, 2009). The red marked wiggle-trace represents the raw pulse. After the filters are applied we can see that the new radar trace has increased amplitude throughout the profile. These changes are visually noticeable throughout the radargram. Additionally, the bandpass filter works by filtering out all frequencies that do not fall in the desired range. For example, I was using a 80 MHz antenna, so I may only want to keep frequencies +/- 40 MHz from 80. This reduces wave frequencies from other sources such as cell phones, electrical power lines, etc.

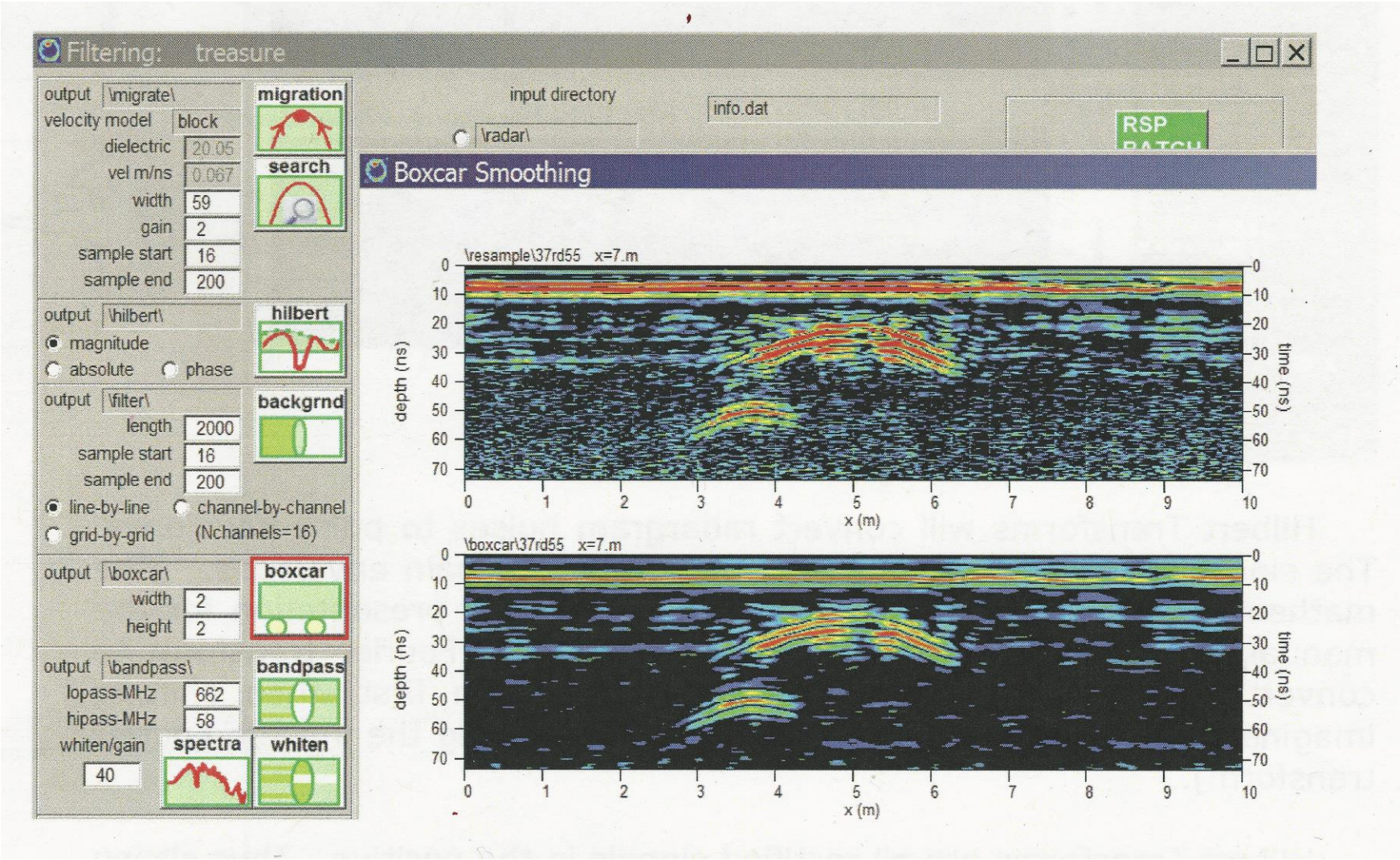

Figure A-3: Example of a boxcar smoothing filter (Goodman, 2009). Boxcar smoothing works by averaging the signal over a given window. It has removed a significant amount of noise in the data.

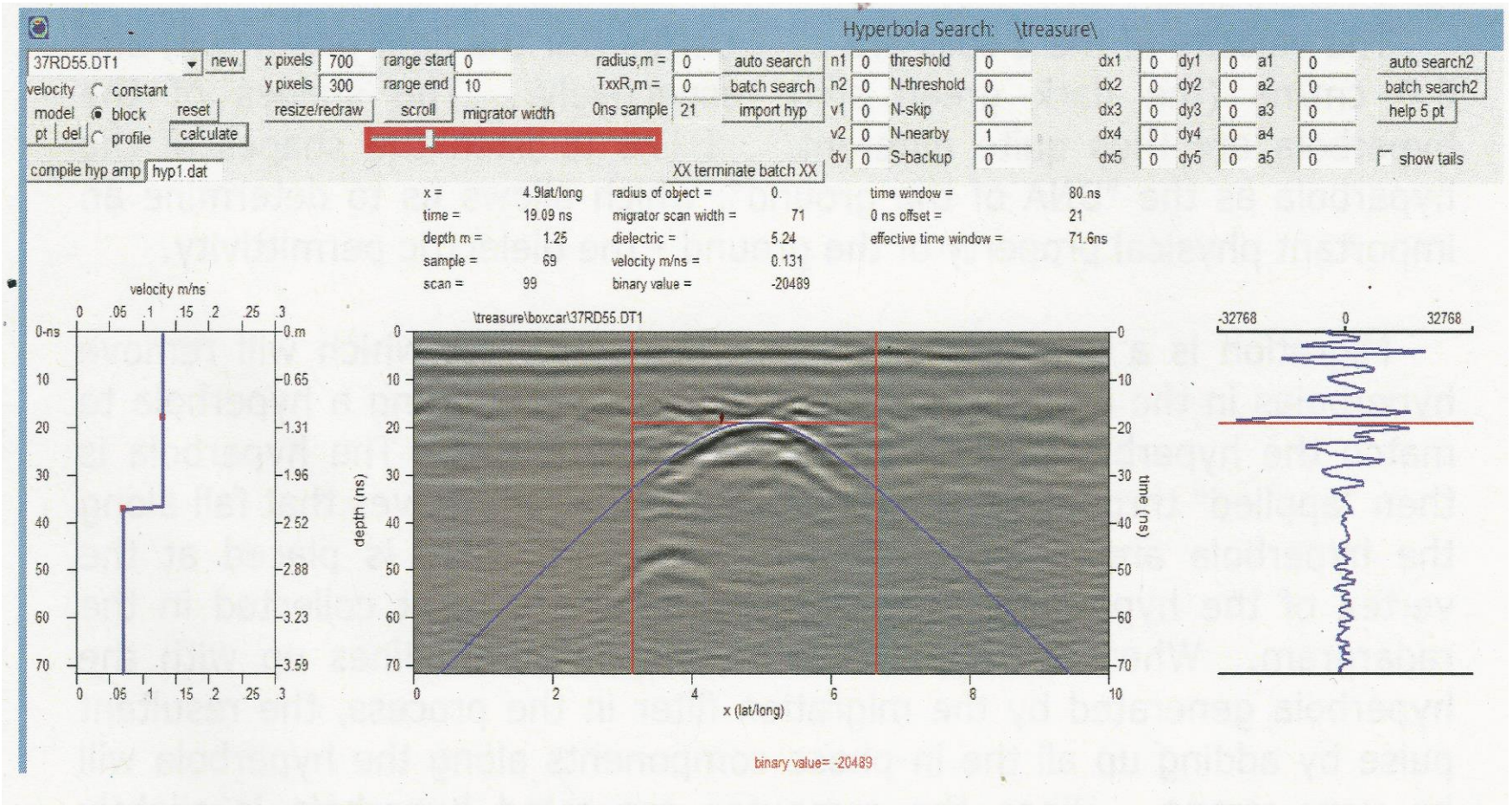

Figure A-4: Example of applying a migration filter (Goodman, 2009). Cylindrical or round objects buried in the ground create hyperbolic reflection patterns. This is because radar pulses spread laterally in a conical shape with depth. Therefore, if an object is a far distance from the GPR unit itself, it may still be received but with a longer two-way travel time. However, if the object is directly below the GPR unit, the two-way travel time will be much faster. Migration is a tool that utilized these hyperbolas to determine wave speed velocity allowing for a correct conversion from time to depth.

Appendix B: Field Measurements

Table B-1: Bedding plane attitude measurements for Seward Park Tertiary bedrock.

South Andrews Bay Outcrop	Kingfisher Point Outcrop	Southeastern Outcrop
S54W, 57N	S73W, 55N	S42W, 62N
S74W, 57N	S70W, 47N	S36W, 66N
S55W, 58N		S65W, 60N
S32W, 72N		
S44W, 62N		
S58W, 65N		
S65W, 66N		

Table B-2: Schmidt hammer results. Mean and standard deviation of uniaxial compressive strength (UCS) values for Seward Park outcrops (Rains, written communication, 2018)

Location	Kingfisher Point Outcrop	South Andrews Bay Outcrop
Standard Deviation	3.3	2.0
Mean	15.0	15.7

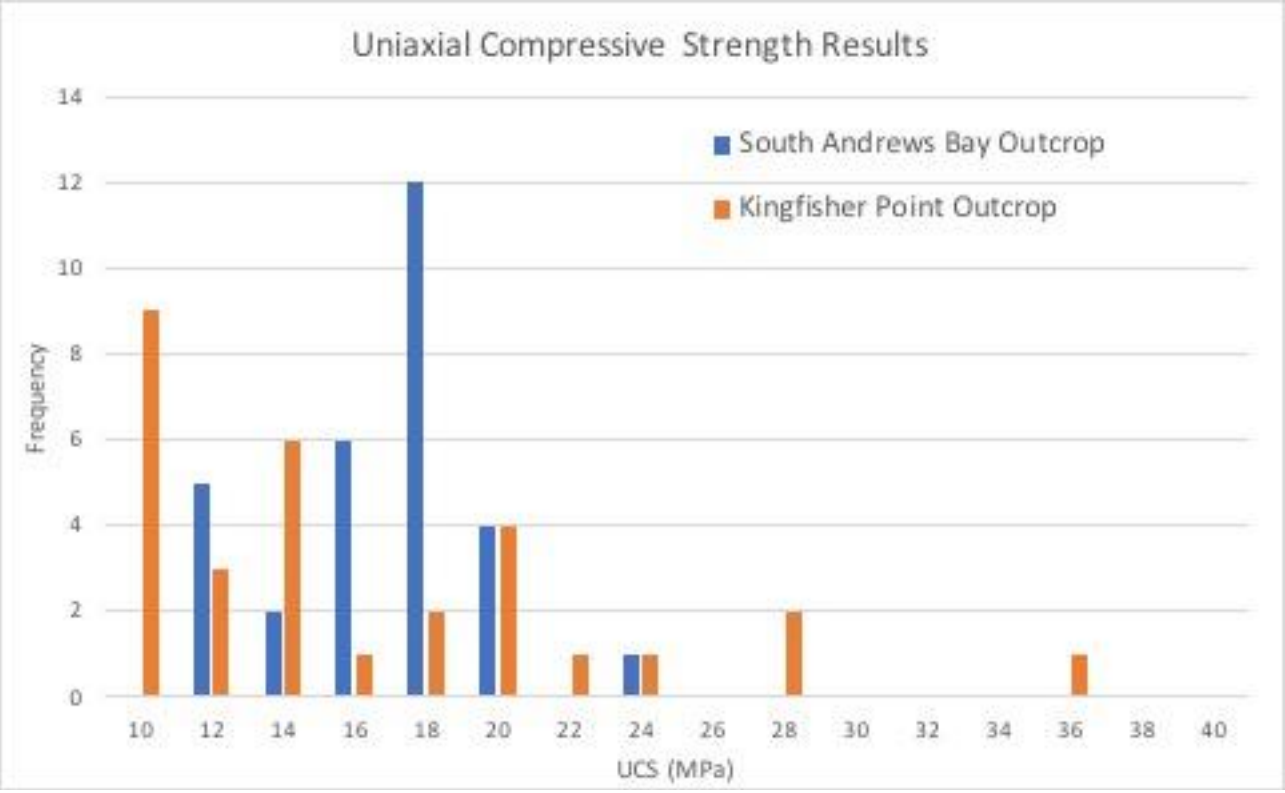

Figure B-1: Schmidt hammer results. Frequency and distribution of uniaxial compressive strength (UCS) values determined from Seward Park Schmidt hammer tests (Rains, written communication, 2018).

Appendix C: Geophysical Survey Information

Table C-1: Ground-penetrating radar survey parameters.

GPR Survey Parameters	
Antenna Frequency	80 MHz
Trace Spacing	0.005 m
Samples/Trace	860
Sampling Interval	0.78125 ns
Signal Position	5.8036 ns
Antenna	GX80 HDR (v.1) =1
Antenna Offset	0.48 m
Time window	671.875 ns
Stacks	1
Wheel	30cm

Table C-2: Survey parameters for the west side (Transect A) seismic line. Geophone spacing interval = 3m.

File Name (.dat)	Shot Location (m)	Delay Time (ms)	Sampling Rate (ms)	Record Length (sec)	Stacking Number	Additional Comments
1001	-5	-40	0.125	1.540	10	
1002	-1.5	-40	0.125	1.540	10	
1003	4.5	-40	0.125	1.540	10	
1004	10.5	-40	0.125	1.540	10	
1005	16.5	-40	0.125	1.540	8	
1006	22.5	-40	0.125	1.540	7	
1007	28.5	-40	0.125	1.540	6	
1008	34.5	-40	0.125	1.540	6	
1009	40.5	-40	0.125	1.540	6	
1010	46.5	-40	0.125	1.540	6	
1011	52.5	-40	0.125	1.540	5	
1012	58.5	-40	0.125	1.540	5	
1013	64.5	-40	0.125	1.540	5	
1014	70.5	-40	0.125	1.540	5	
1015	76.5	-40	0.125	1.540	5	
1016	82.5	-40	0.125	1.540	5	
1017	88.5	-40	0.125	1.540	5	
1018	94.5	-40	0.125	1.540	4	
1019	100.5	-40	0.125	1.540	6	
1020	106.5	-40	0.125	1.540	7	
1021	112.5	-40	0.125	1.540	7	
1022	118.5	-40	0.125	1.540	6	
1023	124.5	-40	0.125	1.540	7	
1024	130.5	-40	0.125	1.540	7	
1025	136.5	-40	0.125	1.540	7	
1026	142.5	-40	0.125	1.540	12	

1027	146	-40	0.125	1.540	12	

Table C-3: Survey Parameters for the east side (Transect B) seismic line. Geophone spacing interval = 2m.

File Name (.dat)	Shot Location (m)	Delay Time (ms)	Sampling Rate (ns)	Record Length (sec)	Stacking Number	Additional Comments
1005	-3	-40	0.125	1.540	5	
1006	22	-40	0.125	1.540	5	
1007	48	-40	0.125	1.540	5	
1008	70	-40	0.125	1.540	10	
1009	94	-40	0.125	1.540	10	
1010	118	-40	0.125	1.540	10	
1011	142	-40	0.125	1.540	10	
1012	166	-40	0.125	1.540	15	
1013	193 (+3)	-40	0.125	1.540	15	

Table C-4: Typical seismic velocities of Quaternary materials (Savage et al., 2000).

Geologic Unit	ρ_{dry} kg/m^3	V_s m/s	V_p m/s	σ	E mPa	μmPa
Recessional Outwash	(1280)	250	630	0.41	225	80
	(1640)	500	760	0.12	917	410
Vashon Till	1920	360	1000	0.43	710	249
	2400	760	1800	0.43	3860	1386
Esperance Sand (Advance Outwash)	(1540)	250	630	0.41	270	96
	1760	500	760	0.12	984	440
Lawton Clay	(1280)	155	1520	0.49	92	31
	(1540)	400	1800	0.47	726	246
Pre-Vashon	1460	340	2040	0.47	1346	458
	(1920)	560	2340	0.47	1770	602

A

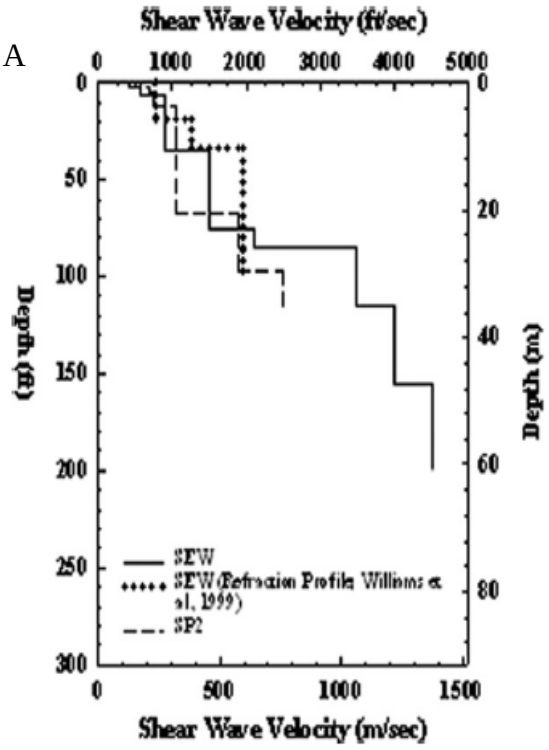

B

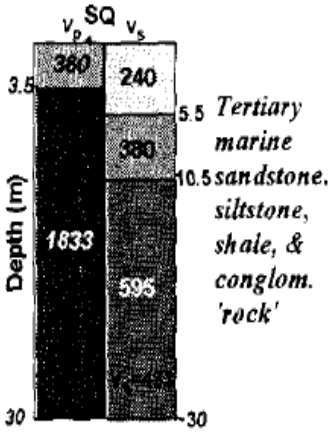

Figure C-1: in-situ velocity measurements of Seward Park Blakeley Formation (Williams et al., 1999; Wong et al., 2014).